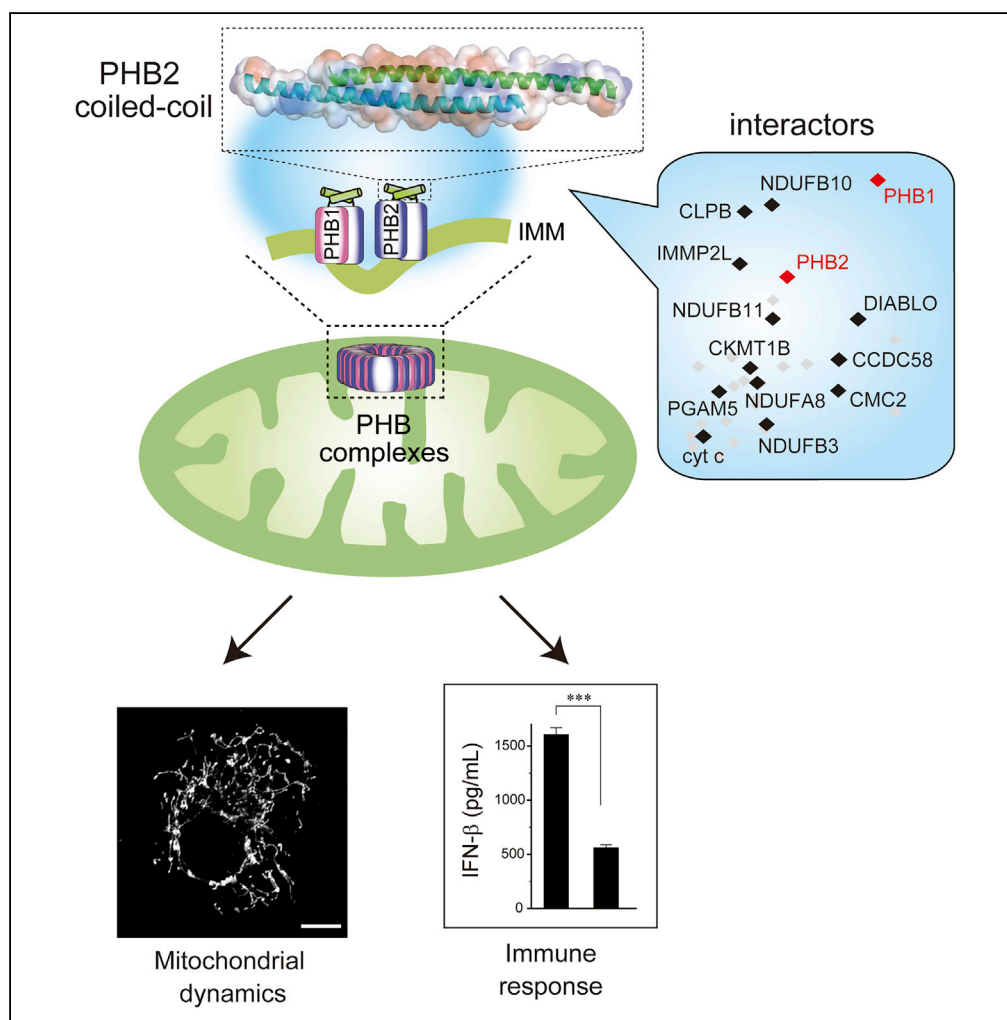## Article

Structural Basis of Mitochondrial Scaffolds by Prohibitin Complexes: Insight into a Role of the Coiled-Coil Region

Takahiro
Yoshinaka,
Hidetaka Kosako,
Takuma
Yoshizumi, ...,
Osamu Kuge, Taro
Tamada, Takumi
Koshiba

koshiba@kyudai.jp

HIGHLIGHTS

Heptad repeat (HR) region
of PHB2 is essential for
PHB complexes in
mitochondria

The HR region of PHB2
assembles into a dimeric,
anti-parallel coiled-coil

Disruption of the PHB2
coiled-coil abolishes
mitochondrial dynamics

The coiled-coil associates
with mitochondrial
proteins, invoking an
immune response

iScience

Article

Structural Basis of Mitochondrial Scaffolds by Prohibitin Complexes: Insight into a Role of the Coiled-Coil Region

Takahiro Yoshinaka,[1] Hidetaka Kosako,[2] Takuma Yoshizumi,[1] Ryo Furukawa,[1] Yu Hirano,[3] Osamu Kuge,[4] Taro Tamada,[3] and Takumi Koshiba[1,5,6,*]

SUMMARY

The coiled-coil motif mediates subunit oligomerization and scaffolding and underlies several fundamental biologic processes. Prohibitins (PHBs), mitochondrial inner membrane proteins involved in mitochondrial homeostasis and signal transduction, are predicted to have a coiled-coil motif, but their structural features are poorly understood. Here we solved the crystal structure of the heptad repeat (HR) region of PHB2 at 1.7-Å resolution, showing that it assembles into a dimeric, antiparallel coiled-coil with a unique negatively charged area essential for the PHB interactome in mitochondria. Disruption of the HR coiled-coil abolishes well-ordered PHB complexes and the mitochondrial tubular networks accompanying PHB-dependent signaling. Using a proximity-dependent biotin identification (BioID) technique in live cells, we mapped a number of mitochondrial intermembrane space proteins whose association with PHB2 relies on the HR coiled-coil region. Elucidation of the PHB complex structure in mitochondria provides insight into essential PHB interactomes required for mitochondrial dynamics as well as signal transduction.

INTRODUCTION

Mitochondria are dynamic organelles that undergo continual cycles of fusion and fission. The balance of these two processes controls the overall morphology of the mitochondrial population, which contains individual organelles ranging from small isolated spheres to interconnected tubular networks (Westermann, 2010; Chan, 2012; Wai and Langer, 2016). Beyond controlling mitochondrial morphology, mitochondrial fusion also enables cooperation between mitochondria and protects the function of the mitochondrial population. Without adequate mitochondrial fusion, mitochondria exist as autonomous organelles, a state that results in greater heterogeneity and dysfunction of the mitochondrial population (Chen et al., 2005). In mammals, mitochondrial fusion is controlled by several conserved large guanosine triphosphatases of the dynamin family that orchestrate mitofusins (MFN1 and MFN2) at the outer mitochondrial membrane (OMM) and optic atrophy 1 (OPA1), having eight isoforms resulting by transcriptional and post-translational processes, in the inner mitochondrial membrane (IMM) (Chen and Chan, 2010).

Prohibitins (PHBs) are ubiquitously expressed IMM proteins that form ring-like PHB complexes comprising multiple PHB1 and PHB2 subunits (Tatsuta et al., 2005) to maintain the cristae structure and mitochondrial integrity (Artal-Sanz and Tavernarakis, 2009; Osman et al., 2009b). Several lines of evidence indicate that PHB complexes act as a functional platform to sequester mitochondrial proteases from the substrate, OPA1, and control proteolytic processing of the OPA1 balance (coexistence with long and short isoforms) to regulate mitochondrial fusion (Merkwirth et al., 2008 & 2012; Ehses et al., 2009; Richter-Dennerlein et al., 2014; Korwitz et al., 2016). In mice, the absence of PHB complexes is embryonic lethal (Merkwirth et al., 2008), and postnatal neuronal-specific ablation of *Phb2* causes neurodegeneration (Merkwirth et al., 2012), defects thought to be linked to the destabilization of fusogenic OPA1. One of the PHB complexes, PHB2, was also recently revealed to act as a crucial receptor for the removal of damaged mitochondria by mitophagy (Wei et al., 2017). Although the embryologic and cellular functions of PHB complexes involved in both mitochondrial morphology and integrity are beginning to be understood, little is known about how these molecules act mechanistically. PHBs have a unique structural motif, a 4,3 hydrophobic heptad repeat ([HR] region: Figure S1A) that is strongly associated with the coiled-coil motif (Figure S1B), which has central roles in protein-protein interactions (Grigoryan and Keating, 2008). The presence of the HR region in mitochondrial proteins is reminiscent of the structure of MFN1, in which the formation of anti-parallel coiled-coil

[1]Department of Biology, Faculty of Science, Kyushu University, Fukuoka 819-0395, Japan

[2]Division of Cell Signaling, Fujii Memorial Institute of Medical Sciences, Tokushima University, Tokushima 770-8503, Japan

[3]Quantum Beam Science Research Directorate, National Institutes for Quantum and Radiological Science and Technology, Ibaraki 319-1106, Japan

[4]Department of Chemistry, Faculty of Science, Kyushu University, Fukuoka 819-0395, Japan

[5]Department of Chemistry, Faculty of Science, Fukuoka University, Fukuoka 814-0180, Japan

[6]Lead Contact

*Correspondence:
koshiba@kyudai.jp

https://doi.org/10.1016/j.isci.2019.08.056

structures mediates mitochondrial tethering (Koshiba et al., 2004). In addition, similar anti-parallel coiled-coils are formed during mitochondrial fission events mediated by dimeric states of mitochondrial division 1 and mitochondrial fission 1 complexes at the OMM (Koirala et al., 2010; Zhang et al., 2012). Understanding how PHB molecules are involved in mitochondrial membrane dynamics via the HR region in their putative coiled-coil motifs will fill a critical gap in our knowledge concerning its actions.

In the present study, we performed a biophysical and cell biologic analysis of the HR region of PHB2. We found that the HR region of PHB2 forms a dimeric antiparallel coiled-coil with a highly charged surface. Surprisingly, in addition to its self-dimerization, we revealed that this coiled-coil motif mediates the tight assembly of the PHB interactome in mitochondria. Mutations that disrupt the HR coiled-coil or change the HR surface charge properties severely disrupt the PHB interactome assembly, as well as mitochondrial morphology and its functions, indicating that PHB complexes are important for mitochondrial integrity. These structural insights contribute to elucidate the mechanistic roles of PHB complexes essential for mitochondrial functions.

RESULTS

Heptad Repeat Region of PHB2 Is Essential for PHB Complexes in Mitochondria

To understand the structural basis of PHB complexes in mitochondria through its HR region, we sought to determine interactors that rely on this region. We first established HEK293 cell lines stably expressing either variant 1 (V1: used as the standard variant in this study) or variant 3 (V3: an alternative splicing variant lacking most of the HR sequence) of PHB2 (Figures S1A and S1B), which harbor a C-terminal biotin ligase (BirA) with a hemagglutinin tag, and screened live cells for proximate and interacting proteins. Validating these BirA-fused PHB2 variants biochemically, both recombinants behaved almost identically to endogenous PHB2, showing its potential localization in the mitochondria (Figure S1C) and association with the membrane (Figure S1D), although the affinity of PHB2(V3)-BirA with the membrane was slightly less than that of the V1 construct. The assembly formation of PHB2(V1)-BirA was also similar to that of endogenous PHB2, and it formed large PHB complexes <1 MDa, as revealed by blue native polyacrylamide gel electrophoresis (BN-PAGE) (Figure S1E). The complex formation of PHB2(V3)-BirA, however, was largely disrupted and exhibited an almost disordered complex state in the mitochondria.

To further characterize these structural differences of the PHB complexes, we used a proximity-based biotin labeling method in live cells. Using the improved proximity-dependent biotin identification screen (BioID2) (Kim et al., 2016) in our established HEK293 cell lines, we followed large-scale pull-downs of biotinylated mitochondrial proteins by mass spectrometric (MS) analysis (Figures 1A and 1B, and Table S1). We detected at least seven overlapping hits (PHB1, PHB2, AFG3L2, YME1L1, TIMM50, NDUFA5, and ATP5B) with previously identified PHB2(V1) interactors (Richter-Dennerlein et al., 2014) (Table S1). Remarkably, comparative analysis between these two variants revealed that a selective group of mitochondrial proteins, including PHB1; several subunits of electron transport chains (ETCs, mostly mitochondrial complex I); caseinolytic peptidase B protein homolog (CLPB), which is also known as mitochondrial ATPases associated with diverse cellular activities (AAA) ATPase chaperonin; and other functional proteins, including proteases, were significantly enriched in the PHB2(V1)-BirA fraction (Figure 1C). These results clearly demonstrated that the assembly of PHB2 with such interactors (an interactome) in mitochondria depended on the HR region.

Structural Profiling of PHB Complexes by Cross-Linking MS

Having identified that well-ordered PHB complexes in mitochondria are responsible for the presence of the HR region, we next applied a chemical cross-linking approach coupled with MS (Leitner et al., 2016) to elucidate the spatial arrangement of the complexes at the subunit level. Isolated mitochondria from cells expressing a Myc-tagged version of PHB2(V1) were chemically cross-linked using an MS-cleavable cross-linker, disuccinimidyl dibutyric urea, the resultant extracts were purified by affinity beads, and the digested peptides were analyzed by liquid chromatography-tandem MS (Figure 1D). We identified a total of 33 unique Lys-Lys cross-links in the PHB complexes (Table S2), and the vast majority of identified peptide pairs were between its heterotypic PHB1-PHB2 (11 cross-links) or homotypic PHB2-PHB2 (8 cross-links) (Figure 1E), suggesting that these molecules tightly interact, consistent with a previous report (Tatsuta et al., 2005). Three pairs of heterotypic peptides in particular (PHB1^{K202}-PHB2^{K216}, PHB1^{K202}-PHB2^{K262}, and PHB1^{K208}-PHB2^{K218}) were substantiated by the results of a reverse cross-linking experiment (using a Myc-tagged version of PHB1 construct, Table S2). We also found an intriguing linkage between PHB2
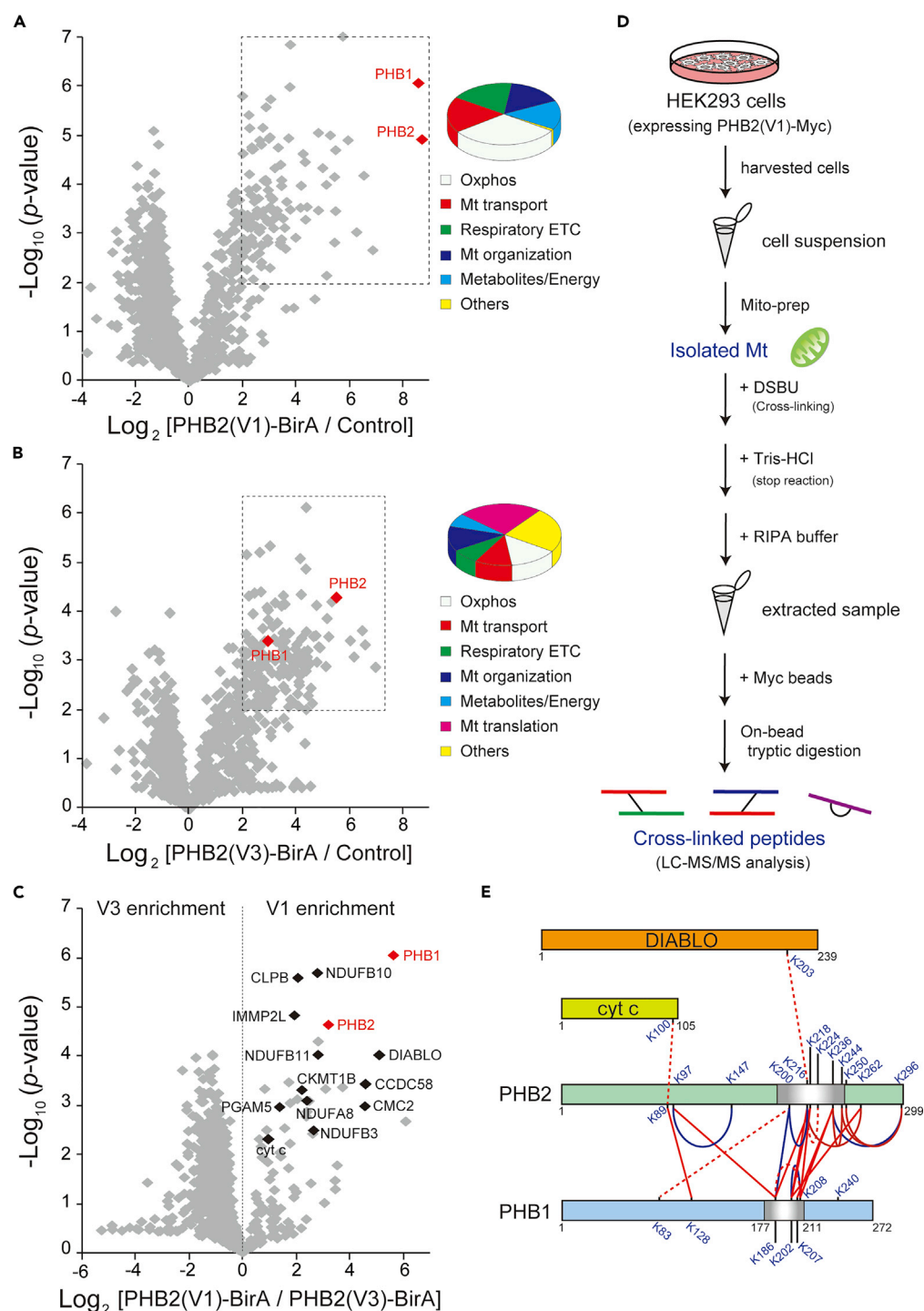
Figure 1. Identification of PHB2 Interactors that Rely on the HR Region

(A–C) Volcano plot showing PHB2(V1)-BirA versus control (A), PHB2(V3)-BirA versus control (B), and PHB2(V1)-BirA versus PHB2(V3)-BirA (C) plotted against the p value of quadruplicate ($n = 4$) experiments. The dashed boxes in (A) and (B) show significantly increased proteins (abundance ratio >4, p < 0.01), and the enrichment proteins (110 for A and 169 for B) were analyzed by gene ontology annotations defining the concepts of the biologic process mapping shown in the pie charts (%) on the right. In (C), proteins annotated with known IMS proteins are indicated in black and the positions of PHB1 and PHB2 are indicated in red. The control cells were the original HEK293 cell lines.

Figure 1. Continued

(D) Schematic view of the chemical cross-linking coupled with mass spectrometry approach. Mitochondria (Mt) from HEK293 cells stably expressing PHB2(V1)-Myc were chemically cross-linked with MS-cleavable cross-linker disuccinimidyl dibutyric urea (DSBU) (maximal distance constraint of 12.5 Å) for 30 min, followed by stringent extraction of the protein lysates. The extracted cross-linked proteins were affinity purified for subsequent analysis and identification by liquid chromatography-tandem MS.

(E) Cross-link map showing the sequence position of all observed Lys-Lys cross-linked pairs between PHB2 and other mitochondrial proteins. Cross-links within PHB2 could not be distinguished either intramolecularly (one monomer) or intermolecularly (monomers) in this analysis. The cross-linking experiments were performed under 50 µM (red dashed line) or 100 µM (blue line) DSBU concentrations, and the red solid lines show cross-linked pairs observed in both conditions.

See also Figure S1, Tables S1 and S2.

(K216) and DIABLO (K203), or between PHB2 (K89) and cytochrome *c* (K100), both of which are involved in apoptosis, suggesting a substantial role of PHB2 in cell death (Merkwirth et al., 2008). Of note, the site-specific interactions in the PHB complexes converged around the HR region (Figure 1E), providing us novel structural insight into the complex formation at the subunit level.

The HR Region of PHB2 Assembles into a Helical, Anti-parallel Coiled-Coil Structure

We investigated the biophysical properties of the HR region of PHB2. Based on the coiled-coil prediction program COILS (Lupas et al., 1991), we expressed a histidine-tagged recombinant protein spanning residues 188–247 (denoted $PHB2^{188-247}$) in bacterial cells. The purified $PHB2^{188-247}$ appeared to be well folded, because circular dichroism analysis indicated that it was highly helical (>60%) and unfolded cooperatively in neutral pH conditions (Figure S2A). As we expected, introducing a proline residue into the polypeptide (I225P) drastically reduced its helicity (Figure 2A).

We obtained crystals of $PHB2^{188-265}$, slightly extended at the C termini, and solved its atomic structure at 1.7 Å by molecular replacement (Table S3). The $PHB2^{188-265}$ polypeptide folded into a dimeric anti-parallel coiled-coil 113 Å long (Figure 2B). Each of the two helices can be depicted in a helical wheel diagram (Figure 2C, left) showing that the *a* and *d* residues of the HR constitute a predominantly hydrophobic interaction interface (Figure 2C, right) with an accessible surface area of 1,430 Å². The PHB2 coiled-coil shows striking structural similarity (folding) to the coiled-coil region of p-stomatin PH1511p (Yokoyama et al., 2008), which is a member of the stomatin/prohibitin/flotillin/HflKC (SPFH) family (Figure S2B).

Role of the HR Region in PHBs Involved in Complex Formation

Our crystal structure revealed that the PHB2 homodimer folds into an elongated shape providing a highly charged surface (Figure S2C, top). A remarkable feature of the coiled-coil is the presence of a negatively charged patch comprising three glutamates (E^{229}, E^{231}, and E^{233}) with a glutamine (Q^{227}) residue at the center of the structure (Figure 2D). To test whether these acidic residues are essential for its coiled-coil folding and/or the PHB complexes in mitochondria, we designed a mutant in which these residues were substituted with lysine (K^{229}, K^{231}, and K^{233}: denoted $PHB2^{KKK}$) (Figure S2C, middle).

The substitution had no effect on the folding properties based on the indistinguishable molar ellipticity at 222 nm between the wild-type (WT) and KKK variant (Figure S2D, orange), indicating similar levels of helicity at the polypeptide level. Moreover, the $PHB2^{KKK}$ substitution in the full-length molecule also co-immunoprecipitated with the same level of endogenous PHBs in HEK293 cells as the WT, whereas the coiled-coil-disrupted variant $PHB2^{I225P}$ mostly lost this ability (Figure S2E). Consistent with these findings, we confirmed using the BioID2 assay (Table S4) that the $PHB2^{KKK}$ variant retained the abilities of heterotypic interaction with PHB1 (abundance ratio; WT/KKK = 1.28, Figure S2F, top). These findings indicate that the negatively charged residues on the HR surface do not affect the physical hydrophobic interaction interface between PHBs and consequently its overall coiled-coil folding. The presence of acidic residues, however, is absolutely required for the formation of the PHB interactome in mitochondria. Monitored by BN-PAGE, the PHB complexes comprising the $PHB2^{KKK}$ variant seemed to be destabilized (Figure S2G), and the BioID2 assay further revealed a much lower association with previously identified mitochondrial intermembrane space (IMS) proteins, such as CLPB and subunits of mitochondrial complex I (NDUFA8, NDUFB3, NDUFB10, and NDUFB11), in the $PHB2^{KKK}$ variant than in the WT (Table S4 and Figure S2F).
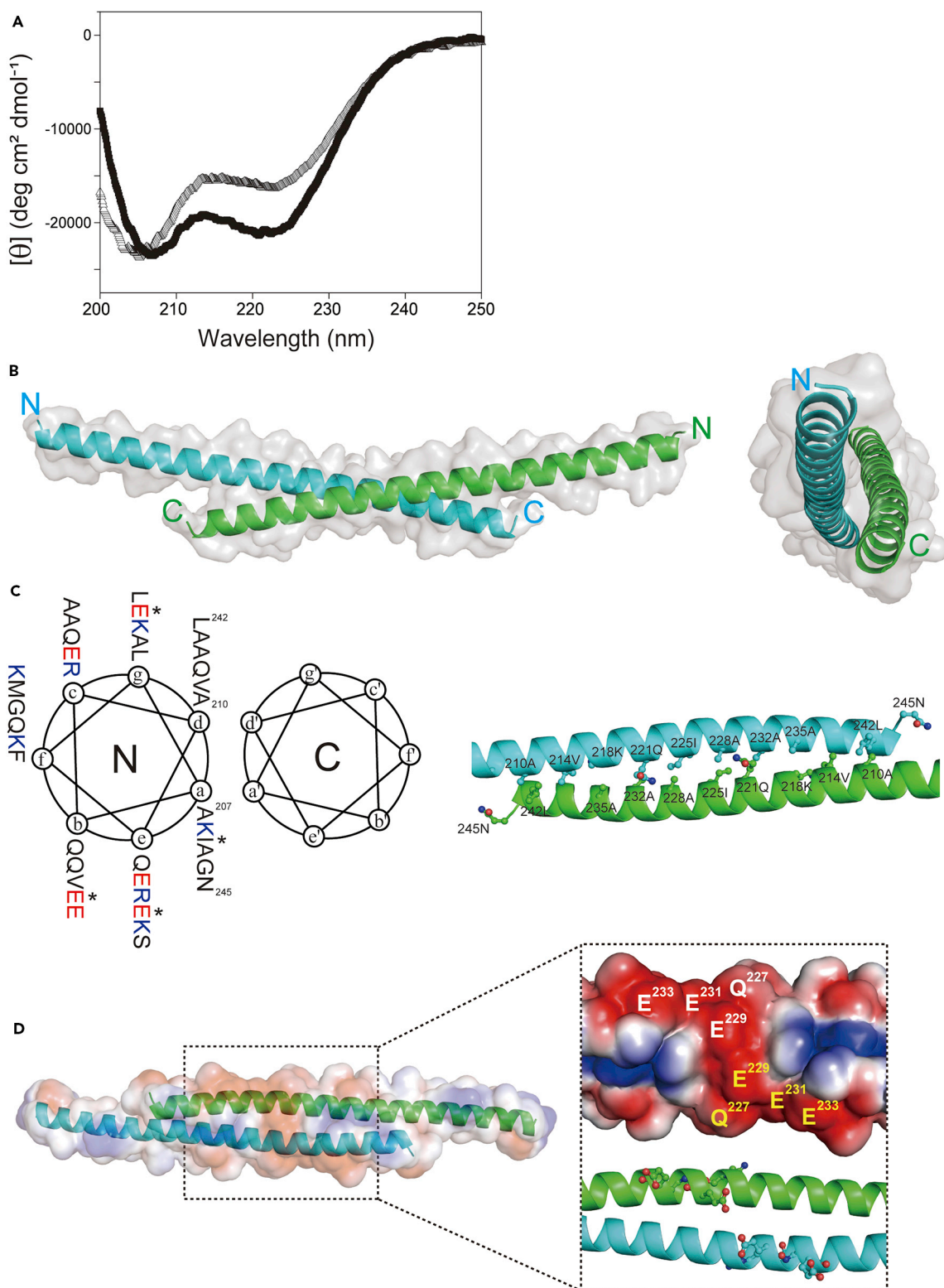
Figure 2. Biophysical Properties of the HR Region of PHB2

(A) Circular dichroism spectra of PHB2$^{188-247}$ (filled square) and its I225P variant (open triangle) at 4°C in 1× PBS (pH 7.4).

(B) The overall structure of PHB2$^{188-265}$. The left panel shows the side view of the dimeric, anti-parallel coiled-coil with the N and C termini labeled and the molecular surface in shadow. The right panel shows an end-on view looking down the 2-fold axis of the dimer structure.

Figure 2. _Continued_

(C) The left panel shows a helical wheel diagram with the residues indicated, and the interface residues from the _a–d_ layers are shown in the right panel. In the left panel, positively and negatively charged residues are shown in blue and red, respectively, and four residues (I^{225}, E^{229}, E^{231}, and E^{233}) that were mutated in this study are indicated with an asterisk.

(D) An electrostatic potential map of $PHB2^{188-265}$. Acidic potential is shown in red, and basic regions are shown in blue. The right panel shows an enlarged view from the central region of the coiled-coil, and the glutamates are projected. The structures in the figure were depicted using PyMOL.

See also Figure S2 and Table S3.

Role of the PHBs/HR Region in Mitochondrial Morphology and Function in Yeast

We thus studied the role of the HR region of PHB2 involved in mitochondrial morphology using _PHB2_-depleted cells. Conditional gene targeting of _Phb2_ in mouse embryonic fibroblast (MEF) cells via Cre recombinase expression had severe effects on the mitochondrial morphology and led to fragmented mitochondria in more than 60% of the cells (Figures 3A and 3B, _flox/flox_ + Cre), as reported previously (Merkwirth et al., 2008). The morphologic defects were restored when the $PHB2^{WT}$ gene, but not the coiled-coil-disrupted variant, $PHB2^{I225P}$, was re-introduced into the null cells. Importantly, the $PHB2^{KKK}$ variant also had little activity for regulating mitochondrial dynamics (Figures 3A and 3B) and a collapsed cristae morphology, as seen in the $PHB2^{I225P}$ variant, monitored by electron microscopy (Figure 3C).

Sequential alignments between PHB2 homologs in different organisms revealed conservation of the glutamate cluster, except for Phb2 of the yeast _Saccharomyces cerevisiae_ (Figure 4A). In yeast, however, Phb1 possesses the conserved glutamates and shows a high probability of the coiled-coil formation (Figure 4B, left), leading us to explore the phenotypic significance of Phb1/HR _in vivo_. Although single _PHB1_ deletion (_phb1Δ_) mutant cells grow at a similar rate to WT cells (Figure 4C, + HygB), deletions of both _PHB1_ and its genetic interactor _PSD1_ (_phb1Δpsd1Δ_) cause lethality (Birner et al., 2003; Osman et al., 2009a) (Figure 4C, + G-418/HygB). The growth defect of the _phb1Δpsd1Δ_ cells was completely rescued by introducing a plasmid encoding WT yeast Phb1 with a C-terminal Myc tag ($Phb1^{WT}$). Most critically, rescue experiments involving the proline ($Phb1^{V202P}$, $Phb1^{V213P}$, and $Phb1^{V202/213P}$) or lysine ($Phb1^{KKK}$) variants showed no detectable restoration of cell growth even with abundant protein expression levels (Figure 4C). Taken together, these comparative _in vitro_ and _vivo_ studies highlight the importance of the coiled-coil and the charged residues within the structure involved in PHB function.

PHB2 Is Involved in Mitochondrial-Mediated Antiviral Innate Immunity

The aforementioned experiments indicated that the HR region of PHBs had potential roles in mitochondrial morphology and growth of yeast. To evaluate the physiologic relevance of PHB complexes in mammalian cells, we investigated the role of PHB2 via its HR region on a mitochondrial-mediated antiviral innate immune response, the retinoic acid-inducible gene I (RIG-I) signaling pathway, which is a vital function of mitochondria (Seth et al., 2005; Koshiba et al., 2011; Koshiba, 2013). We verified that $Phb2^{flox/flox}$ MEFs challenged with Sendai virus (SeV), a negative-stranded RNA virus of the Paramyxoviridae family, potently activated RIG-I-mediated signal transduction and the cells produced interferon β (IFN-β) and a proinflammatory cytokine interleukin-6, but the immune responses were attenuated when the Cre recombinase was expressed in the cells (Figure S3A). In contrast, the _Phb2_-depleted MEFs were rescued by introduction of the $PHB2^{WT}$ gene, but neither $PHB2^{I225P}$ nor $PHB2^{KKK}$ substantially recovered the antiviral responses. The functionality of the _Phb2_-depleted MEFs, however, was unaffected when the cells were infected with a double-stranded DNA virus, Herpes simplex virus 1, which activates the cGAS/STING cytosolic DNA sensing pathway (Figure S3B). Moreover, cytochrome _c_ oxidase (COX, complex IV) activity was not affected in the _Phb2_-depleted MEFs (Figure S3C, brown stain). These observations indicate that the HR region contributes to the PHB2-mediated execution of mitochondrial-dependent antiviral innate immunity (RIG-I pathway).

To understand how PHB2 regulates RIG-I-mediated antiviral innate immunity, we focused on the functional role of the HR-dependent PHB2-interacting proteins involved in signal transduction using an RNA interference approach. HEK293 cells treated with each of the 12 gene candidates identified by BioID2 (Table S4) with its gene-specific small interfering RNAs (siRNAs), and activation of the IFN-β reporter was triggered by the delivery of poly(I:C), a synthetic analog of viral double-stranded RNA, into the siRNA-treated cells by transient transfection. Among these candidates, we confirmed that specific targeting of the subunits of mitochondrial complex I (_NDUFA8_, _NDUFB3_, and _NDUFB11_) potently suppressed activation of the IFN-β luciferase reporter (Figure 5A), consistent with our previous findings (Yoshizumi et al., 2017). Knockdown
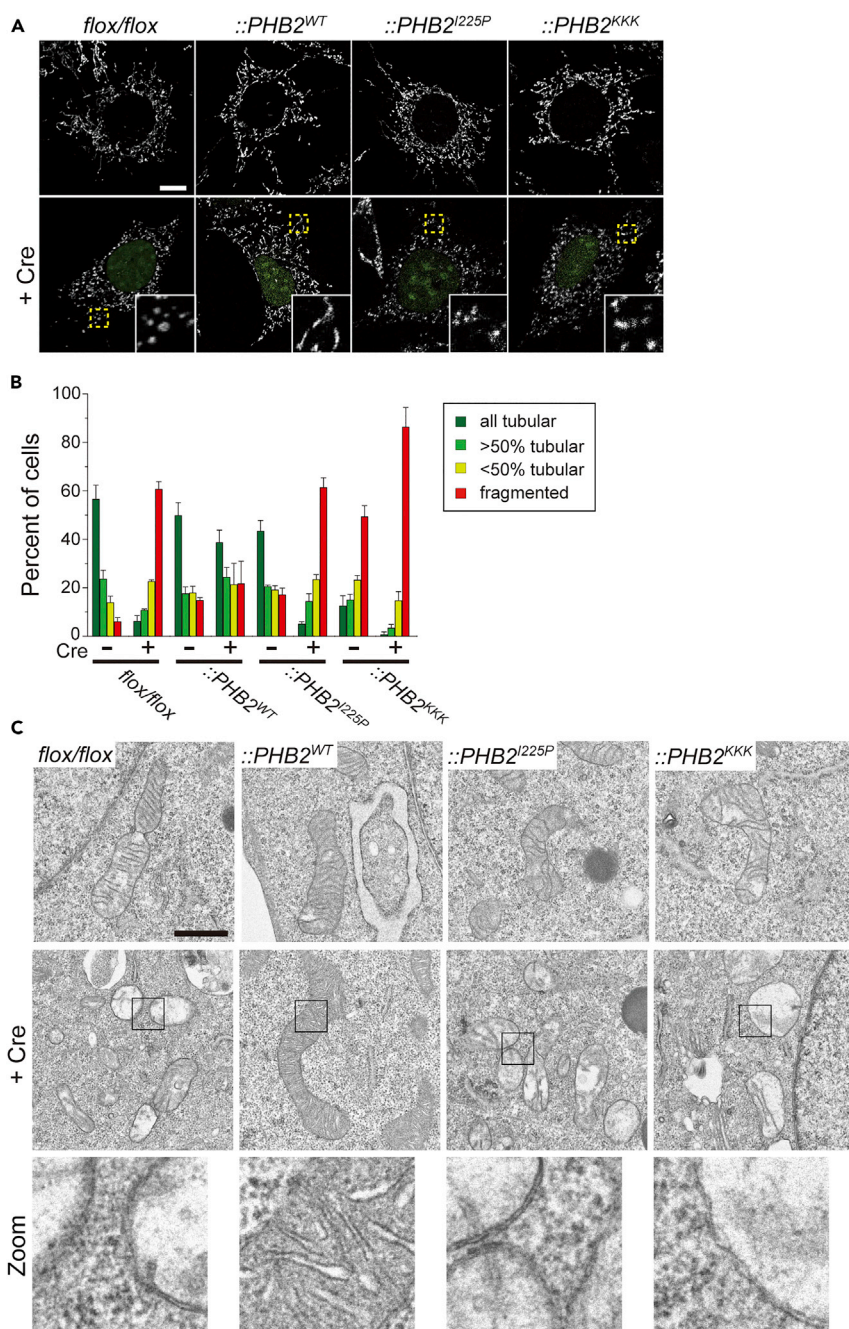
Figure 3. Disruption of PHB2 Coiled-Coil Abolishes Mitochondrial Dynamics

(A and B) *Phb2$^{flox/flox}$* and its variant MEFs were infected with or without a retrovirus encoding GFP-fused Cre recombinase (+Cre) for 72 h to deplete the endogenous *Phb2* gene, and the mitochondrial morphology of each cell was monitored by immunofluorescence microscopy (A). Mitochondria in cells were visualized using an antibody against mtHsp70. Insets depict the magnified images of each yellow boxed area. Scale bar, 10 μm. In (B) quantification of data in (A) is shown. Cells were scored as one of four morphologic categories as depicted on the right. In these experiments, at least 100 cells were scored. Each value represents the mean ± SEM (*n* = 3 experiments).

(C) *Phb2$^{flox/flox}$* and its variant MEFs were infected with or without a retrovirus encoding Cre recombinase (+Cre) for 72 h to deplete the endogenous *Phb2* gene, and the mitochondrial ultrastructure of each cell was analyzed by transmission electron microscopy. Bottom images: higher magnification images of regions outlined in the middle panels. Scale bar, 1 μm.
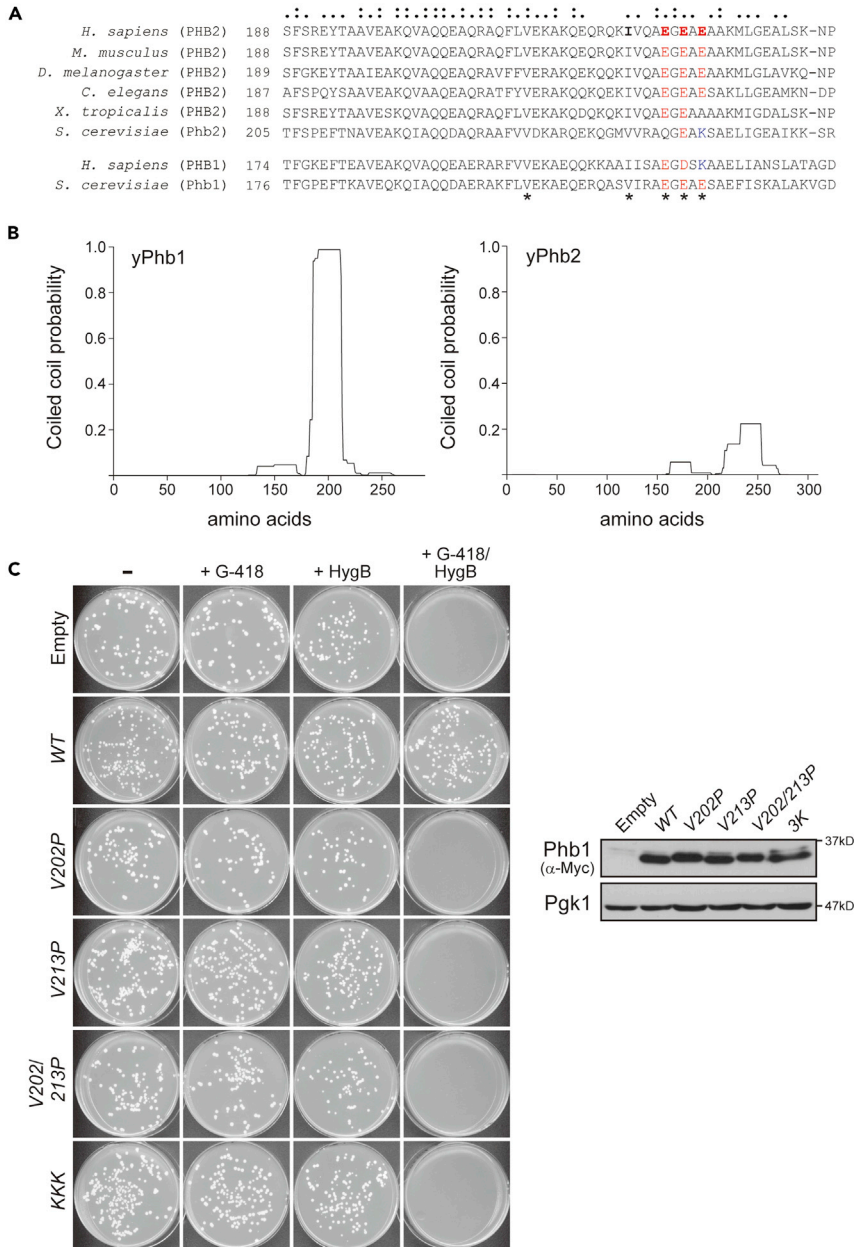
See also Figure S3.

Figure 4. Highly Conserved Glutamic Acid Residues in the HR Coiled-Coil Are Essential for the Function of PHB2 Homologs in Yeast

(A) Alignment of prohibitin homologs (*Homo sapiens*, *Mus musculus*, *Drosophila melanogaster*, *Caenorhabditis elegans*, *Xenopus tropicalis*, and *Saccharomyces cerevisiae*) around the HR region. Colons (:) indicate conserved residues among all species shown in the figure, and dots (·) indicate residues with similar properties. Asterisks at the bottom of the alignment sequences indicate mutated amino acids in the study.

(B) Prediction results of coiled-coil probability of yeast Phb1 (left) and Phb2 (right) using the program COILS (Lupas et al., 1991). The yPhb1 coiled-coil is predicted to be highly probable relative to that of yPhb2.

(C) Heterozygous diploid strains (*PSD1/psd1Δ::kanMX4 PHB1/phb1Δ::hphNT1 CAN1/can1Δ::STE2pr-Sp_his5*) carrying pRS416 (Empty), pRS416/yPhb1WT-Myc (*WT*), pRS416/yPhb1V202P-Myc (*V202P*), pRS416/yPhb1V213P-Myc (*V213P*), pRS416/yPhb1V202/213P-Myc (*V202/213P*), and pRS416/yPhb1KKK-Myc (*KKK*) were allowed to sporulate, plated on the various selection media indicated, and incubated at 30°C for 3 days. All the media contained canavanine without histidine and uracil for the selection of *MATα* haploid strains carrying pRS416 or its derivatives. + G-418, selection for *psd1Δ* strains; + HygB, selection for *phb1Δ* strains. The right panels show protein levels in the heterozygous diploid cells analyzed by western blot with antibodies against the Myc epitope and 3-phosphoglycerate kinase (Pgk1).
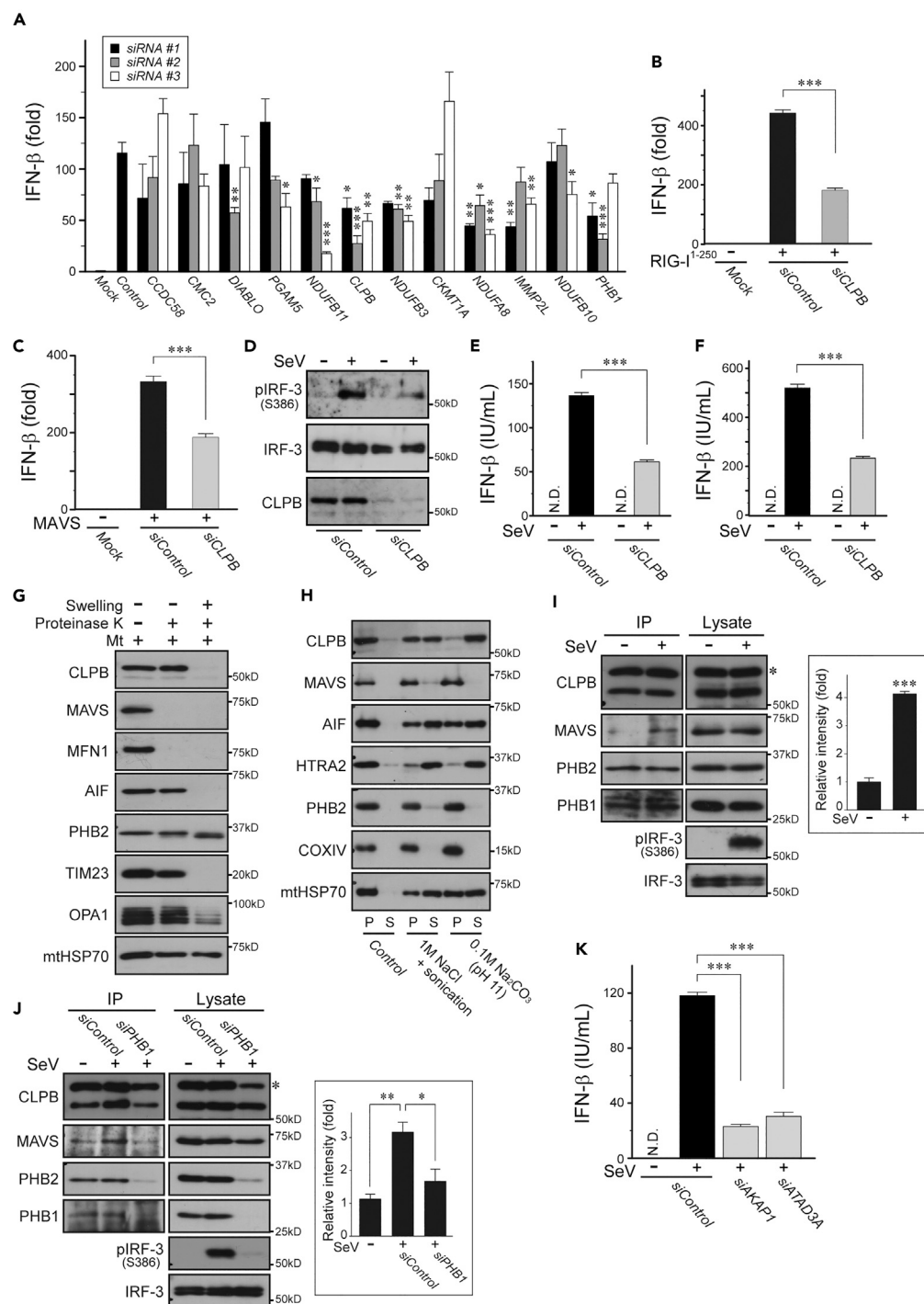
Figure 5. Involvement of PHB Complexes in Antiviral Innate Immunity via CLPB

(A) Activation of the IFN-β reporter in siRNA-treated HEK293 cells (each target RNAi; #1–#3) transfected without (Mock) or with poly(I:C).

(B and C) HEK293 cells treated with control or *CLPB* siRNAs were transfected with IFN-β luciferase reporter plasmid either with RIG-I$^{1-250}$ (B) or MAVS (C) expression plasmids (Mock; empty vector). The transfected cells were analyzed 24 h later for IFN-β-dependent luciferase activity.

(D) The siRNA-treated HEK293 cells were mock infected (−) or infected with SeV (4 hemagglutinin (HA) units/mL) for 20 h, and the activation of endogenous IRF-3 was analyzed by immunoblotting with its specific antibody against the phosphorylation of Ser^{386} site (pIRF-3). Anti-IRF-3 was used as the loading control.

Figure 5. Continued

(E and F) (E) Experiments were performed similarly to those in (D), except that the amounts of IFN-β produced by the infected cells were measured by ELISA. In (F), A549 cells were used instead of HEK293 cells. N.D., not detected.

(G) The mitochondrial fraction (Mt) isolated from HEK293 cells was treated with proteinase K (50 μg/mL) under regular (−) or hypotonic swelling (+) conditions for 15 min on ice. The reactants were developed by immunoblotting with antibodies against CLPB or against several mitochondrial markers as indicated. OMM proteins: MAVS and MFN1. IMS proteins: AIF and PHB2. IMM proteins: TIM23 and OPA1. Matrix protein: mtHSP70.

(H) Isolated mitochondria from HEK293 cells were treated with either 1 M NaCl (plus sonication) or 0.1 M Na_2CO_3 (pH 11.0) for 30 min on ice. After centrifugation, the supernatant (S) and pellets (P) were analyzed by immunoblotting with antibodies against CLPB or against several mitochondrial proteins as indicated.

(I) Interaction of CLPB and MAVS. HEK293 cells stably expressing Myc-tagged CLPB were mock infected (−) or infected with SeV (4 HAU/mL) for 20 h, and postnuclear cell lysates were subjected to immunoprecipitation (IP) with the antibody against Myc followed by analysis of western blots with an antibody against MAVS. The asterisk indicates Myc-tagged CLPB. The graph on the right shows the quantification of MAVS bands from the IP fraction analyzed by densitometry.

(J) Experiments were performed similarly to those in (I), except that the cells used in the study were pre-treated with control or *PHB1* siRNAs before SeV infection.

(K) Experiments were performed similarly to those in (E), except that the cells were pre-treated with siRNA against *AKAP1* or *ATAD3A*.

Each value represents the mean ± SEM (*n* = 3 experiments). Statistical analysis was performed by the two-tailed Student's t test. ***p < 0.001, **p < 0.01, and *p < 0.05. See also Figures S4 and S5 and Tables S4 and S5.

of *PHB1* was also sufficient to inhibit RIG-I-mediated antiviral signaling, as seen with depletion of homolog *Phb2* in MEFs. In particular, CLPB preferentially impaired the RIG-I-mediated antiviral innate immunity among these candidates (Figure 5A).

CLPB Bridges PHB2 to the Mitochondrial Adaptor, Mitochondrial Antiviral Signaling Protein

We therefore evaluated the functional role of the PHB2-CLPB axis involved in mitochondrial-mediated antiviral innate immunity. Overexpression of N-terminal CARD domains of RIG-I (designated as RIG-I$^{1-250}$) in HEK293 cells induced a robust intracellular antiviral response, as reported previously (Seth et al., 2005; Yasukawa et al., 2009), and the activation was attenuated when the cells were treated with the *CLPB*-specific siRNA (Figure 5B). Knockdown of endogenous CLPB in cells similarly reduced the activation of the IFN-β reporter in response to overexpression of the mitochondrial antiviral signaling protein (MAVS) (Figure 5C), an OMM protein that acts downstream of RIG-I (Seth et al., 2005). Affirmatively, virus-induced phosphorylation of endogenous interferon regulatory factor-3 (IRF-3), the hallmark of IRF-3 activation (Mori et al., 2004), was severely impaired in the *CLPB*-depleted cells relative to control cells (Figure 5D), and the production of endogenous IFN-β protein was similarly reduced (Figure 5E). We also corroborated the observed effects of CLPB using another type of cell, A549 (Figure 5F). In contrast, loss of endogenous CLPB did not impair the IRF-3 phosphorylation in response to extracellular poly(I:C), which activates the mitochondrial-independent toll-like receptor 3 (TLR-3) pathway (Figure S4A); furthermore, mitochondria in the *CLPB*-depleted cells were healthy with a mitochondrial membrane potential (Figure S4B) and COX activity (Figure S4C) indistinguishable from those control cells. Taken together, these results demonstrated that CLPB likely acts as a modulator downstream of MAVS in the RIG-I signaling pathway.

We performed a structure-function analysis to fill the topologic gap between CLPB and the mitochondrial adaptor MAVS. Biochemical experiments revealed that sub-mitochondrial localization of CLPB was the IMS because protease accessibility in isolated mitochondria from cells increased only when the OMM was disrupted by hypotonic swelling (Figure 5G). Sonication of mitochondria with high-salt conditions (1 M NaCl) or treatment of mitochondria with an alkaline solution (pH 11.0) allowed us to extract CLPB from the exclusively soluble fractions (Figure 5H), similar to unanchored IMS proteins, such as apoptosis-inducing factor or HtrA serine peptidase 2. Consistent with this fact, we confirmed that the CLPB associated with many kinds of IMS proteins (Table S5) and physically interacted with PHB2 via its putative coiled-coil motif at the central region (Figure S5A). Together, these behaviors indicate that CLPB is a soluble IMS protein that does not embed into the IMM.

Mechanistic Investigation of the Mitochondrial Signalosome

We attempted to clarify how CLPB, as a part of PHB complexes, is involved in the RIG-I signaling pathway. To address this issue, we analyzed immunoprecipitates derived from HEK293 cells to determine whether CLPB could functionally and physically interact with MAVS. Despite the fact that CLPB, which was tightly

associated with PHB complexes, barely interacted with endogenous MAVS under physiologic conditions, its interactions were markedly enhanced by SeV infection (Figure 5I). The observed role of CLPB-PHB complexes in antiviral immunity was also verified by PHB2 immunoprecipitation (Figure S5B). Using a co-immunoprecipitation approach, we mapped the region of MAVS that interacts with CLPB through its transmembrane region (Figures S5C and S5D), assuming that their interfaces would present at the IMS. Importantly, the virus-induced MAVS-CLPB interactions were abolished when the PHB proteins were depleted by siRNA (Figure 5J), suggesting that the scaffold function of the PHB complexes is required for the phenomenon.

Finally, we explored additional molecules that might tether CLPB and MAVS at the IMS. By performing BioID2 experiments in HEK293 cells stably expressing either CLPB or MAVS harboring BirA tags, we identified several molecules that were highly enriched in both fractions (also filtered by PHB complexes, Figure S5E and Table S5). Of these, we were interested in two mitochondrial proteins, A-kinase-anchoring protein 1 (AKAP1) in which the N terminus is localized to the IMS (Jun et al., 2016) and ATPase family AAA-domain containing protein 3 A (ATAD3A) that spans the IMM and OMM (Baudier, 2018) (Figure S5F). Consistent with the findings, AKAP1 and ATAD3A both co-immunoprecipitated with endogenous MAVS in the HEK293 cells (Figure S5G), and depletion of these molecules in the cells exhibited strikingly defective antiviral innate immune responses against SeV infection (Figure 5K). We assume that both AKAP1 and ATAD3A tether MAVS throughout the infection process because the BioID2 analysis revealed that these interactions were similar following SeV infection (Figure S5H). Taken together, these results demonstrated that CLPB bridges PHB complexes (IMM) and MAVS (OMM) with the assistance of AKAP1 and ATAD3A at the IMS and invokes an immune response from the mitochondrial signalosome (Figure S5I).

DISCUSSION

PHBs are key components of mitochondrial scaffold proteins that localize in the IMM from yeast to mammals. PHB belongs to the SPFH family of proteins that also function as membrane scaffolds by forming highly ordered oligomers in many species (Browman et al., 2007). Although several biochemical analyses suggest that coiled-coil motifs at their C terminus are required for PHB oligomerization and its functions (Joshi et al., 2003; Tatsuta et al., 2005; He et al., 2008), direct evidence for their roles in mitochondrial functions via the structural motif is limited. Here we show that the HR region at the C terminus of PHB2 forms a dimeric, anti-parallel coiled-coil revealed by X-ray crystallography and demonstrated their involvement in mitochondrial morphology and especially, in antiviral innate immunity (RIG-I pathway).

Our biochemical analysis indicates that the HR region of PHB2, in addition to serving as a homotypic dimerization, mediates a strong interaction with their same region in PHB1 (Table S2 and Figure 1E), which is assumed to fold into a heterotypic dimer (Merkwirth and Langer, 2009). In fact, our simulation of the heterotypic dimerization model predicts proper folding without any structural constraints, and notably, the coiled-coil also showed a negatively charged patch (Figure S2C, bottom), an essential feature for PHB2 *in vitro* and *vivo* functions. Although our results demonstrate that the formation of PHB complexes in mitochondria is HR dependent, it should be noted that the interactions between PHB proteins seem to be quite complex, because some weak interactions are still observed in variants without the coiled-coils (Table S1 and Figure S2E). Indeed, a previous study demonstrated that an SPFH domain protein from archaea *Pyrococcus horikoshii* implied its successive self-oligomerization without the coiled-coil region (Kuwahara et al., 2009). In future work, it will be important to unravel the relative contributions of these multiple interactions in the PHB complexes and how they affect the interactome assembly.

Besides the role of PHBs in mitochondrial integrity, several studies have pointed to the function of these proteins in viral infection, especially an association with viral proteins (Kuadkitkan et al., 2010; Wintachai et al., 2012; Liu et al., 2015). In this context, we found that PHB complexes are involved in RIG-I-mediated antiviral innate immunity via CLPB (Figure 5), an interactor of the PHB2 coiled-coil motif. Our previous study revealed that RIG-I-mediated antiviral innate immunity requires oxidative phosphorylation activity, a prominent physiologic function of mitochondria, and OPA1 ensures the activity and regulates the immune response (Yoshizumi et al., 2017). Consistent with the fact, the interactome assembly of mitochondrial PHB complexes includes several subunits of ETC (Tables S1, S4, and S5), and ablation of these specific genes in cells attenuates RIG-I-mediated signal transduction (Figure 5A). Based on these findings together, we propose a mechanistic model of the role of PHB complexes in mediating virus-triggered innate immune signal transduction (Figure S5I). In this model, a topologic gap between MAVS and the PHB complexes is

filled by CLPB, with the assistance of AKAP1 and ATAD3A, that builds a bridge between the OMM and IMM upon viral infection, forming an MAVS signalosome that leads to the recruitment of various downstream effectors, such as tumor necrosis factor receptor-associated factor family members on the OMM (West et al., 2011; Koshiba, 2013). Our biochemical and structural insights might help to clarify how PHB complexes mediate mitochondrial-mediated innate immunity.

Finally, CLPB variants are reported in humans with autosomal recessive mitochondrial disorders (Saunders et al., 2015; Wortmann et al., 2015; Pronicka et al., 2017), although the exact physiologic functions of the protein remain elusive. On the other hand, the bacterial homolog clpB acts as a chaperone involved in the disaggregation of misfolded proteins (Doyle and Wickner, 2009). The findings of the present study may pave the way for understanding the unexpected role of CLPB in structural rearrangements of MAVS, ultimately leading to an activated conformation, and mutations of CLPB may affect to fulfill this role.

Limitations of the Study

We demonstrated that CLPB bridges PHB complexes (IMM) and MAVS (OMM) with the assistance of AKAP1 and ATAD3A at the IMS and invokes mitochondrial-mediated antiviral innate immunity. In the present study, however, we could not determine whether these interactions (MAVS-CLPB-AKAP1-ATAD3A) are direct or indirect. Because MAVS is a C-terminal-tail-anchored OMM protein with few amino acids facing into the IMS, we cannot exclude the possibility that additional molecules, such as mitochondrial contact site and cristae-organizing system (MICOS) complex (Rampelt et al., 2017), mediate accessible contact sites between the IMM and OMM and assist in establishing the mitochondrial signalosome. Indeed, our BioID2 data revealed that both MAVS and CLPB substantially associate with many MICOS components (Table S5). Further studies to elucidate the mechanistic and functional roles of these MICOS components will improve our understanding of how PHB interactomes are involved in MAVS signaling, particularly the linkage between mitochondrial physiology and innate immunity. Finally, because the prominent function of MAVS signaling is precisely regulated upon viral infection, it is also crucial to clarify how the mitochondrial signalosome is inactivated or terminated by inhibitors such as MFN2 (Yasukawa et al., 2009; Sasaki et al., 2013). Our study did not capture the whole mitochondrial signalosome during the infection process, and additional BioID studies of the kinetics under viral infection will reveal the transient structural rearrangement and provide clues regarding the communication between PHB interactomes and MFNs.

METHODS

All methods can be found in the accompanying Transparent Methods supplemental file.

SUPPLEMENTAL INFORMATION

Supplemental Information can be found online at https://doi.org/10.1016/j.isci.2019.08.056.

AUTHOR CONTRIBUTIONS

T. Yoshinaka, T. Yoshizumi, and T.K. performed most of the mammalian cell culture experiments. R.F., Y.H., and T.T. performed bacterial expression, purification of recombinant proteins, and CD experiments. Y.H. and T.T. crystalized the recombinant protein and determined its crystal structure. O.K. performed the yeast

iScience

CellPress

study and H.K. performed the BioID2 and XL-MS analyses. All the authors analyzed the data and interpreted all the experimental results. T.K. designed experiments and wrote the manuscript.

DECLARATION OF INTERESTS

The authors declare no competing interests.

REFERENCES

Artal-Sanz, M., and Tavernarakis, N. (2009). Prohibitin and mitochondrial biology. Trends Endocrinol. Metab. 20, 394–401.

Baudier, J. (2018). ATAD3 proteins: brokers of a mitochondria-endoplasmic reticulum connection in mammalian cells. Biol. Rev. Camb. Philos. Soc. 93, 827–844.

Birner, R., Nebauer, R., Schneiter, R., and Daum, G. (2003). Synthetic lethal interaction of the mitochondrial phosphatidylethanolamine biosynthetic machinery with the prohibitin complex of Saccharomyces cerevisiae. Mol. Biol. Cell 14, 370–383.

Browman, D.T., Hoegg, M.B., and Robbins, S.M. (2007). The SPFH domain-containing proteins: more than lipid raft markers. Trends Cell Biol. 17, 394–402.

Chan, D.C. (2012). Fusion and fission: interlinked processes critical for mitochondrial health. Annu. Rev. Genet. 46, 265–287.

Chen, H., and Chan, D.C. (2010). Physiological functions of mitochondrial fusion. Ann. N. Y. Acad. Sci. 1201, 21–25.

Chen, H., Chomyn, A., and Chan, D.C. (2005). Disruption of fusion results in mitochondrial heterogeneity and dysfunction. J. Biol. Chem. 280, 26185–26192.

Doyle, S.M., and Wickner, S. (2009). Hsp104 and ClpB: protein disaggregating machines. Trends Biochem. Sci. 34, 40–48.

Ehses, S., Raschke, I., Mancuso, G., Bernacchia, A., Geimer, S., Tondera, D., Martinou, J.C., Westermann, B., Rugarli, E.I., and Langer, T. (2009). Regulation of OPA1 processing and mitochondrial fusion by m-AAA protease isoenzymes and OMA1. J. Cell Biol. 187, 1023–1036.

Grigoryan, G., and Keating, A.E. (2008). Structural specificity in coiled-coil interactions. Curr. Opin. Struct. Biol. 18, 477–483.

He, B., Feng, Q., Mukherjee, A., Lonard, D.M., DeMayo, F.J., Katzenellenbogen, B.S., Lydon, J.P., and O'Malley, B.W. (2008). A repressive role for prohibitin in estrogen signaling. Mol. Endocrinol. 22, 344–360.

Joshi, B., Ko, D., Ordonez-Ercan, D., and Chellappan, S.P. (2003). A putative coiled-coil domain of prohibitin is sufficient to repress E2F1-mediated transcription and induce apoptosis. Biochem. Biophys. Res. Commun. 312, 459–466.

Jun, Y.W., Park, H., Lee, Y.K., Kaang, B.K., Lee, J.A., and Jang, D.J. (2016). D-AKAP1a is a signal-anchored protein in the mitochondrial outer membrane. FEBS Lett. 590, 954–961.

Kim, D.I., Jensen, S.C., Noble, K.A., Kc, B., Roux, K.H., Motamedchaboki, K., and Roux, K.J. (2016). An improved smaller biotin ligase for BioID proximity labeling. Mol. Biol. Cell 27, 1188–1196.

Koirala, S., Bui, H.T., Schubert, H.L., Eckert, D.M., Hill, C.P., Kay, M.S., and Shaw, J.M. (2010). Molecular architecture of a dynamin adaptor: implications for assembly of mitochondrial fission complexes. J. Cell Biol. 191, 1127–1139.

Korwitz, A., Merkwirth, C., Richter-Dennerlein, R., Tröder, S.E., Sprenger, H.G., Quirós, P.M., López-Otín, C., Rugarli, E.I., and Langer, T. (2016). Loss of OMA1 delays neurodegeneration by preventing stress-induced OPA1 processing in mitochondria. J. Cell Biol. 212, 157–166.

Koshiba, T. (2013). Mitochondrial-mediated antiviral immunity. Biochim. Biophys. Acta 1833, 225–232.

Koshiba, T., Detmer, S.A., Kaiser, J.T., Chen, H., McCaffery, J.M., and Chan, D.C. (2004). Structural basis of mitochondrial tethering by mitofusin complexes. Science 305, 858–862.

Koshiba, T., Yasukawa, K., Yanagi, Y., and Kawabata, S. (2011). Mitochondrial membrane potential is required for MAVS-mediated antiviral signaling. Sci. Signal. 4, ra7.

Kuadkitkan, A., Wikan, N., Fongsaran, C., and Smith, D.R. (2010). Identification and characterization of prohibitin as a receptor protein mediating DENV-2 entry into insect cells. Virology 406, 149–161.

Kuwahara, Y., Unzai, S., Nagata, T., Hiroaki, Y., Yokoyama, H., Matsui, I., Ikegami, T., Fujiyoshi, Y., and Hiroaki, H. (2009). Unusual thermal disassembly of the SPFH domain oligomer from Pyrococcus horikoshii. Biophys. J. 97, 2034–2043.

Leitner, A., Faini, M., Stengel, F., and Aebersold, R. (2016). Crosslinking and mass spectrometry: an integrated technology to understand the structure and function of molecular machines. Trends Biochem. Sci. 41, 20–32.

Liu, S., Wang, W., Brown, L.E., Qiu, C., Lajkiewicz, N., Zhao, T., Zhou, J., Porco, J.A., Jr., and Wang, T.T. (2015). A novel class of small molecule compounds that inhibit hepatitis C virus infection by targeting the prohibitin-CRaf pathway. EBioMedicine 2, 1600–1606.

Lupas, A., Van Dyke, M., and Stock, J. (1991). Predicting coiled coils from protein sequences. Science 252, 1162–1164.

Merkwirth, C., and Langer, T. (2009). Prohibitin function within mitochondria: essential roles for cell proliferation and cristae morphogenesis. Biochim. Biophys. Acta 1793, 27–32.

Merkwirth, C., Dargazanli, S., Tatsuta, T., Geimer, S., Löwer, B., Wunderlich, F.T., von Kleist-Retzow, J.C., Waisman, A., Westermann, B., and Langer, T. (2008). Prohibitins control cell proliferation and apoptosis by regulating OPA1-dependent cristae morphogenesis in mitochondria. Genes Dev. 22, 476–488.

Merkwirth, C., Martinelli, P., Korwitz, A., Morbin, M., Brönneke, H.S., Jordan, S.D., Rugarli, E.I., and Langer, T. (2012). Loss of prohibitin membrane scaffolds impairs mitochondrial architecture and leads to tau hyperphosphorylation and neurodegeneration. PLoS Genet. 8, e1003021.

Mori, M., Yoneyama, M., Ito, T., Takahashi, K., Inagaki, F., and Fujita, T. (2004). Identification of Ser-386 of interferon regulatory factor 3 as critical target for inducible phosphorylation that determines activation. J. Biol. Chem. 279, 9698–9702.

Osman, C., Haag, M., Potting, C., Rodenfels, J., Dip, P.V., Wieland, F.T., Brügger, B., Westermann, B., and Langer, T. (2009a). The genetic interactome of prohibitins: coordinated control of cardiolipin and phosphatidylethanolamine by conserved regulators in mitochondria. J. Cell Biol. 184, 583–596.

Osman, C., Merkwirth, C., and Langer, T. (2009b). Prohibitins and the functional compartmentalization of mitochondrial membranes. J. Cell Sci. 122, 3823–3830.

Pronicka, E., Ropacka-Lesiak, M., Trubicka, J., Pajdowska, M., Linke, M., Ostergaard, E., Saunders, C., Horsch, S., van Karnebeek, C., Yaplito-Lee, J., et al. (2017). A scoring system predicting the clinical course of CLPB defect based on the foetal and neonatal presentation of 31 patients. J. Inherit. Metab. Dis. 40, 853–860.

Rampelt, H., Zerbes, R.M., van der Laan, M., and Pfanner, N. (2017). Role of the mitochondrial

contact site and cristae organizing system in membrane architecture and dynamics. Biochim. Biophys. Acta *1864*, 737–746.

Richter-Dennerlein, R., Korwitz, A., Haag, M., Tatsuta, T., Dargazanli, S., Baker, M., Decker, T., Lamkemeyer, T., Rugarli, E.I., and Langer, T. (2014). DNAJC19, a mitochondrial cochaperone associated with cardiomyopathy, forms a complex with prohibitins to regulate cardiolipin remodeling. Cell Metab. *20*, 158–171.

Sasaki, O., Yoshizumi, T., Kuboyama, M., Ishihara, T., Suzuki, E., Kawabata, S., and Koshiba, T. (2013). A structural perspective of the MAVS-regulatory mechanism on the mitochondrial outer membrane using bioluminescence resonance energy transfer. Biochim. Biophys. Acta *1833*, 1017–1027.

Saunders, C., Smith, L., Wibrand, F., Ravn, K., Bross, P., Thiffault, I., Christensen, M., Atherton, A., Farrow, E., Miller, N., et al. (2015). CLPB variants associated with autosomal-recessive mitochondrial disorder with cataract, neutropenia, epilepsy, and methylglutaconic aciduria. Am. J. Hum. Genet. *96*, 258–265.

Seth, R.B., Sun, L., Ea, C.K., and Chen, Z.J. (2005). Identification and characterization of MAVS, a mitochondrial antiviral signaling protein that activates NF-κB and IRF3. Cell *122*, 669–682.

Tatsuta, T., Model, K., and Langer, T. (2005). Formation of membrane-bound ring complexes by prohibitins in mitochondria. Mol. Biol. Cell *16*, 248–259.

Wai, T., and Langer, T. (2016). Mitochondrial dynamics and metabolic regulation. Trends Endocrinol. Metab. *27*, 105–117.

Wei, Y., Chiang, W.C., Sumpter, R., Jr., Mishra, P., and Levine, B. (2017). Prohibitin 2 is an inner mitochondrial membrane mitophagy receptor. Cell *168*, 224–238.

West, A.P., Shadel, G.S., and Ghosh, S. (2011). Mitochondria in innate immune responses. Nat. Rev. Immunol. *11*, 389–402.

Westermann, B. (2010). Mitochondrial fusion and fission in cell life and death. Nat. Rev. Mol. Cell Biol. *11*, 872–884.

Wintachai, P., Wikan, N., Kuadkitkan, A., Jaimipuk, T., Ubol, S., Pulmanausahakul, R., Auewarakul, P., Kasinrerk, W., Weng, W.Y., Panyasrivanit, M., et al. (2012). Identification of prohibitin as a Chikungunya virus receptor protein. J. Med. Virol. *84*, 1757–1770.

Wortmann, S.B., Ziętkiewicz, S., Kousi, M., Szklarczyk, R., Haack, T.B., Gersting, S.W., Muntau, A.C., Rakovic, A., Renkema, G.H., Rodenburg, R.J., et al. (2015). CLPB mutations cause 3-methylglutaconic aciduria, progressive brain atrophy, intellectual disability, congenital neutropenia, cataracts, movement disorder. Am. J. Hum. Genet. *96*, 245–257.

Yasukawa, K., Oshiumi, H., Takeda, M., Ishihara, N., Yanagi, Y., Seya, T., Kawabata, S., and Koshiba, T. (2009). Mitofusin 2 inhibits mitochondrial antiviral signaling. Sci. Signal. *2*, ra47.

Yokoyama, H., Fujii, S., and Matsui, I. (2008). Crystal structure of a core domain of stomatin from *Pyrococcus horikoshii* illustrates a novel trimeric and coiled-coil fold. J. Mol. Biol. *376*, 868–878.

Yoshizumi, T., Imamura, H., Taku, T., Kuroki, T., Kawaguchi, A., Ishikawa, K., Nakada, K., and Koshiba, T. (2017). RLR-mediated antiviral innate immunity requires oxidative phosphorylation activity. Sci. Rep. *7*, 5379.

Zhang, Y., Chan, N.C., Ngo, H.B., Gristick, H., and Chan, D.C. (2012). Crystal structure of mitochondrial fission complex reveals scaffolding function for mitochondrial division 1 (Mdv1) coiled coil. J. Biol. Chem. *287*, 9855–9861.

Supplemental Information

Structural Basis of Mitochondrial

Scaffolds by Prohibitin Complexes: Insight

into a Role of the Coiled-Coil Region

Takahiro Yoshinaka, Hidetaka Kosako, Takuma Yoshizumi, Ryo Furukawa, Yu Hirano, Osamu Kuge, Taro Tamada, and Takumi Koshiba

Figure S1, related to Figure 1. Schematic of PHB2 splice variants in humans

(A) Schematic representation of the exon-intron structure of the human *PHB2* genome (top), and their translated two alternative splicing variants, V1 and V3, are shown. The V1 variant encodes a canonical sequence expressed with its complete polypeptide (middle), whereas the V3 variant lacks exon 6, abolishing the putative HR region (highlighted by gray) of the translated protein (bottom). The amino acid positions are indicated above the structure, and the dashed lines indicate the missing amino acids.

(B) Prediction results of the coiled-coil probability of PHB2 variants using the program COILS (Lupas et al., 1991). The V3 variant is predicted to not form the coiled-coil folding (right).

(C) Subcellular localization of BirA-fused constructs of PHB2 variants. The PHB2(V1)-BirA or PHB2(V3)-BirA constructs (HA-epitope-tagged at their C-terminus) were expressed in MEFs, and immunofluorescence against the HA epitope (left) was used to identify the V1- or V3-expressing cells and to determine their subcellular localizations (right). Mitochondria in the same cells were identified by staining with a monoclonal antibody against mtHsp70 (middle). Scale bar, 10 μm.

(D) Isolated mitochondria from HEK293 cells stably expressing either HA-tagged PHB2(V1)-BirA or PHB2(V3)-BirA were treated with either 1 M NaCl (plus sonication) or 0.1 M Na_2CO_3 (pH 11.0) for 30 min on ice. After centrifugation, the supernatant (S) and pellets (P) were analyzed by immunoblotting with antibodies against HA or against several mitochondrial proteins as indicated.

(E) Mitochondria isolated from HEK293 cells stably expressing either HA-tagged PHB2(V1)-BirA or PHB2(V3)-BirA were solubilized in BN-PAGE lysis buffer containing 0.5% (w/v) digitonin and analyzed by BN-PAGE and immunoblotted using the HA-, PHB2-, and TOM40-specific antibodies (left 3 panels). The abundance of BirA-fused proteins in each sample was confirmed by SDS-PAGE in parallel (right panels).
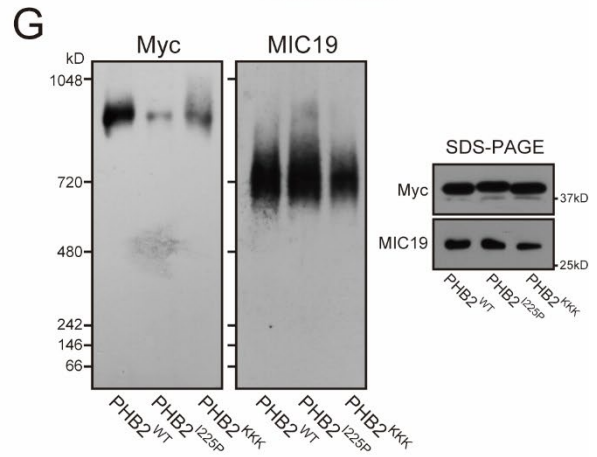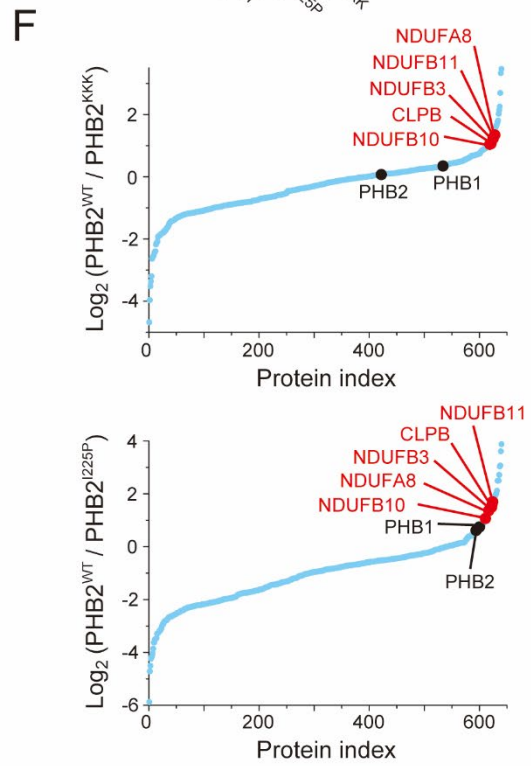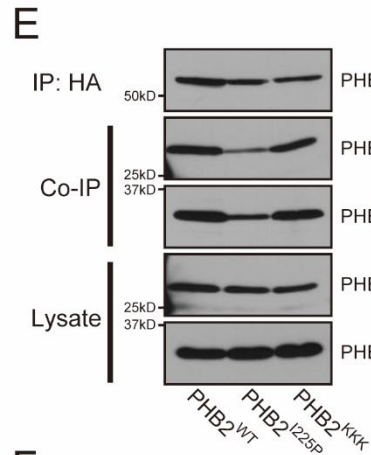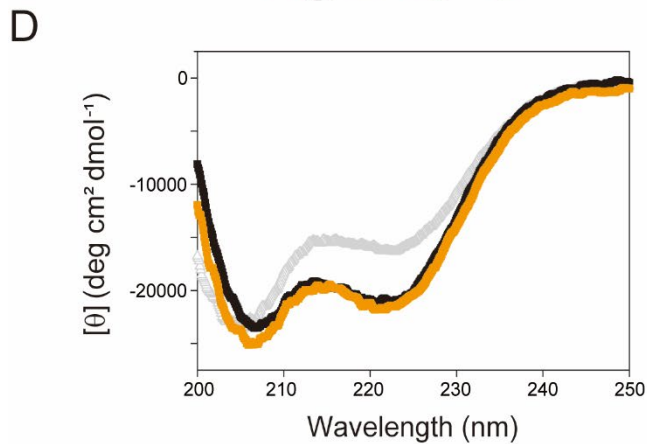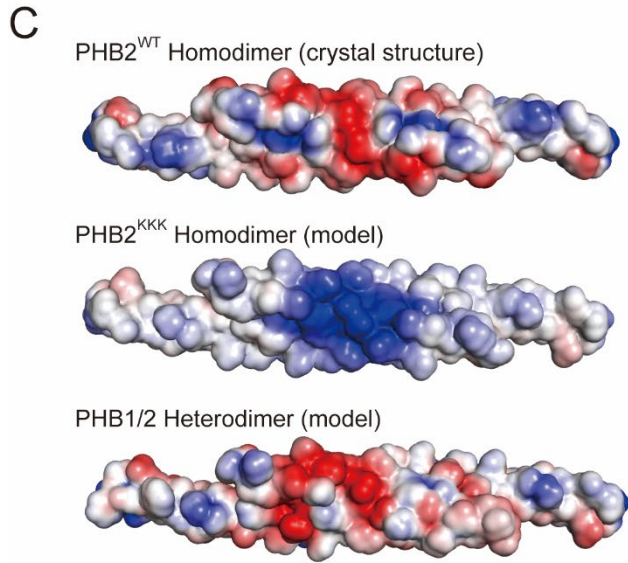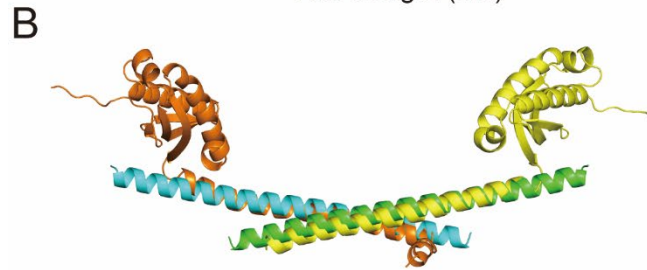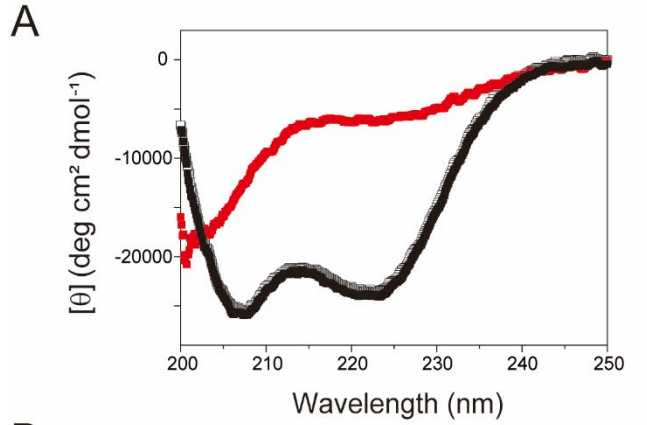
Figure S2, related to Figure 2. Characteristics of the HR region of PHB2

(A) CD spectra of PHB2$^{188-247}$. The sample at 4° C (filled square) was elevated temperature (1° C /min) at 60° C (red square), and then cooled down to 4° C (open square). CD spectra of PHB2$^{188-247}$ in far-UV region (200-250 nm) were measured at these different temperatures at pH 7.2.

(B) Superposition of the PHB2 coiled-coil and the coiled-coil region of p-stomatin PH1511p (PDB ID: 3BK6). Both structures are folded into a crystallographic two-fold symmetry, and the p-stomatin PH1511p anti-parallel dimers are shown in orange and yellow.

(C) An electrostatic potential map of the HR coiled-coil of PHB2 shows a highly charged surface (top). We designed a mutant (PHB2^{KKK}) in which three glutamic acid residues (E^{229}, E^{231}, and E^{233}) were substituted with lysine residues to remove the negatively-charged patch from the center of the structure (middle: model structure). Predicted PHB1-PHB2 heterodimer, which also forms a negative cluster, is shown (bottom: model structure). Basic regions are shown in blue, and acidic regions are shown in red.

(D) CD spectra of WT PHB2$^{188-247}$ (filled square) and its KKK variant (orange square) at 4° C in 1× PBS (pH 7.2). The CD spectrum of I225P variant was overlaid (gray triangle).

(E) Interaction of PHB2 variants with endogenous PHB1 or PHB2. Lysates of HEK293 cells stably expressing HA-tagged PHB2-BirA (WT) and its variants (I225P and KKK) were subjected to immunoprecipitation (IP) with HA monoclonal antibody followed by the analysis of immunoblots (Co-IP) with antibodies against PHB1 or PHB2.

(F) PHB2 coiled-coil is required to form the PHBs interactome assembly. A total of 640 proteins identified from BioID2 experiments (see Table S4) were plotted according to the abundance ratios (log$_2$) of PHB2^{WT}/PHB2^{KKK} (top) or PHB2^{WT}/PHB2^{I225P} (bottom) against individual proteins (Protein index) sorted by their ratios in ascending order.

(G) PHB2 coiled-coil is required to form the PHBs interactome assembly. Mitochondria isolated from HEK293 cells stably expressing Myc-tagged PHB2 (WT) and its variants (I225P and KKK) were solubilized in BN-PAGE lysis buffer containing 0.5% (w/v) digitonin, and analyzed by BN-PAGE and immunoblotted using the Myc- and MIC19-specific antibodies (left 2 panels). The abundance of the Myc-tagged proteins in each sample was confirmed by SDS-PAGE in parallel (right panel).
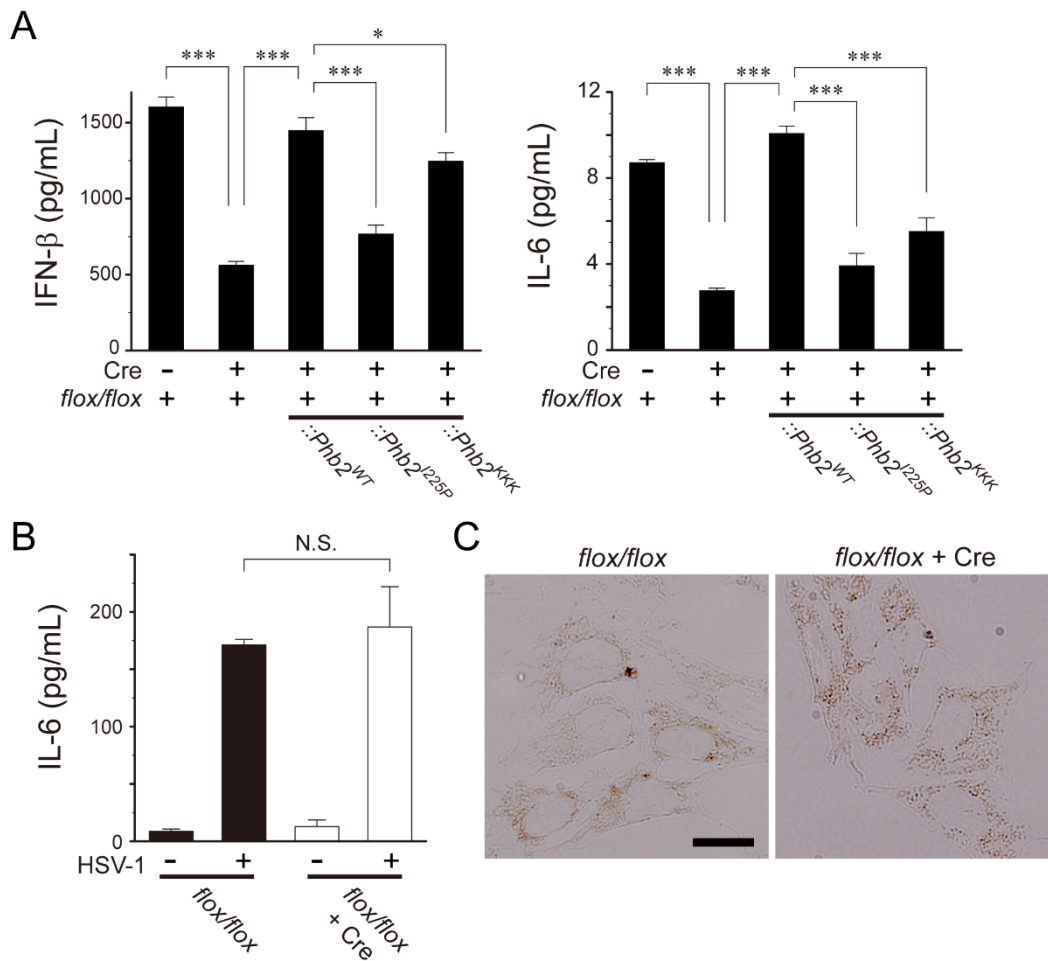
Figure S3, related to Figure 3. Defective RIG-I pathway in *Phb2*-depleted cells

(A) *Phb2flox/flox* and its variant MEFs were infected with SeV [4 hemagglutinin (HA) units/mL] for 18 h, and the cell-free supernatants were analyzed by ELISA to measure the amount of IFN-β (left) or IL-6 (right) secretion.

(B) *Phb2flox/flox* MEFs (± Cre) were infected with HSV-1 (7×10^4 PFU) for 20 h, and the cell-free supernatants were analyzed by ELISA to measure the amount of IL-6 secretion. Each value represents the mean ± SEM (n = 3 experiments). Statistical analysis was performed using the two-tailed Student's *t* test. ****p* < 0.001 and **p* < 0.05, respectively. N.S., not significant.

(C) Comparison of COX activity between *Phb2*-depleted (+ Cre) and the control (left) MEFs. Cells expressing COX activity were indicated by a brown color. Scale bar, 20 μm.
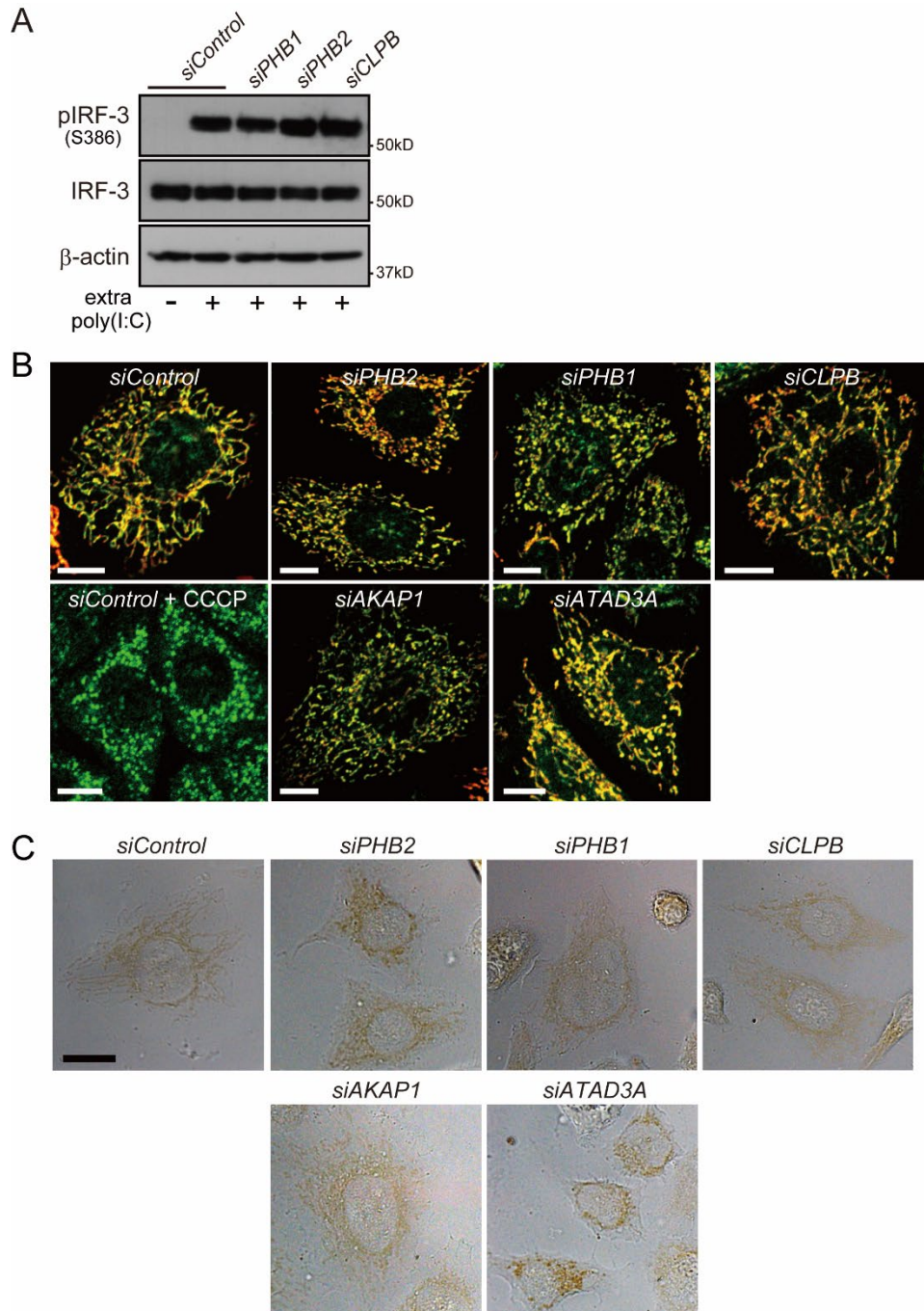
Figure S4, related to Figure 5. Functionality of siRNA-treated cells

(A) HEK293 cells stably expressing TLR-3 were treated with control or indicated siRNAs and the cells were stimulated with extracellular poly(I:C) (2 μg) for 16 h.   Activation of endogenous IRF-3 was analyzed by Western blotting with antibody against phosphorylation of the Ser^{386} site (pIRF-3).   Anti-β-actin was used as the loading control.

(B) The siRNA-treated HeLa cells (as indicated) were stained with MitoTracker Red CMXRos,

which detects the mitochondrial membrane potential ($\Delta\Psi_m$), and mitochondria in the same cells were stained with an anti-COXIV monoclonal antibody (green).　We confirmed that the siRNA-treated cells were uniformly detected with MitoTracker Red (highlighted in yellow), whereas CCCP-treated cells (bottom left panel) failed to stain with the dye, indicating loss of $\Delta\Psi_m$.　Scale bar, 10 μm.

(C) Similar to (B), except that the COX activity of siRNA-treated cells was monitored.　Cells expressing COX activity are indicated by the brown color.　Scale bar, 20 μm.

A

CLPB
ANK1 ANK2 ANK3 ANK4   AAA domain   677

CLPBΔCC
279 308   AAA domain   677

Coiled coil probability

amino acids

Mock CLPB-Myc CLPBΔCC-Myc

37kD   IP: α-Myc
        IB: α-PHB2

37kD   Lysate
        IB: α-PHB2

50kD   IP: α-Myc
        IB: α-Myc

B

IP   Lysate
SeV − +   − +

PHB2   * 37kD

MAVS   75kD

CLPB   50kD

pIRF-3
(S386)   50kD

IRF-3   50kD

C

CARD Pro-rich   TM
HA-MAVS   HA 1 10 77 103 173   540
HA-MAVS(ΔTM) HA
HA-MAVS(ΔCARD/Pro)   HA 201   514

HA-MAVS (full)   + − − −
HA-MAVS (ΔTM)   − + − −
HA-MAVS (ΔCARD/Pro)   − − + −
CLPB-Myc   − + + +

IP: α-Myc
IB: α-HA

100kD
75kD
50kD

Lysate
IB: α-HA

100kD
75kD
50kD

IP: α-Myc
IB: α-Myc

50kD

D

HA-MAVS HA-MAVS (ΔTM) HA-MAVS (ΔCARD/Pro)

HA

Phb2

Merge

E

MAVS 257
CLPB 114   35   PHB1 144

−Log10 (p-value)

AKAP1
ATAD3A

Log2 [PHB2(V1)-BirA / Control]

F

Swelling   − − +
Proteinase K   − + +
Mt   + + +

AKAP1   150kD

ATAD3A   75kD
  *   37kD

MFN2   75kD

AIF   75kD

mtHSP70   75kD

G

AKAP1-Myc   ATAD3A-Myc
      − +   − +

75kD IP: α-Myc   75kD IP: α-Myc
      IB: α-MAVS   IB: α-MAVS

75kD Lysate   75kD Lysate
      IB: α-MAVS   IB: α-MAVS

      IP: α-Myc   75kD IP: α-Myc
150kD IB: α-Myc   IB: α-Myc

H

Log2 (SeV / mock)

MARCH-V
cIAP1
TRAF2
RIG-I

ATAD3A AKAP1

Protein index

I

AKAP1 CARD   MAVS
PRO
OMM
IMS   CLPB CLPB   ATAD3A
IMM   PHB1 PHB2

viral infection →   MAVS signalosome   → RIG-I signaling

PHB complexes

IMS   Complex I
IMM
Matrix

Figure S5, related to Figure 5. Involvement of PHB complexes in antiviral innate immunity via CLPB with its binding partners

(A) Interaction of endogenous PHB2 with CLPB. HEK293 cells were transfected with empty vector (Mock) or plasmids encoding the indicated CLPB constructs (top cartoon), and the lysates were subjected to immunoprecipitation (IP) with an anti-Myc antibody followed by analysis of Western blots with anti-PHB2 antibody. Graph at the bottom left shows the prediction results of the coiled-coil probability of CLPB using the program COILS.

(B) HEK293 cells stably expressing Myc-tagged PHB2 were mock-infected (-) or infected with SeV (4 HAU/mL) for 20 h, and postnuclear cell lysates were subjected to immunoprecipitation (IP) with the antibody against Myc followed by Western blot analysis with the antibody against MAVS. Asterisk indicates Myc-tagged PHB2.

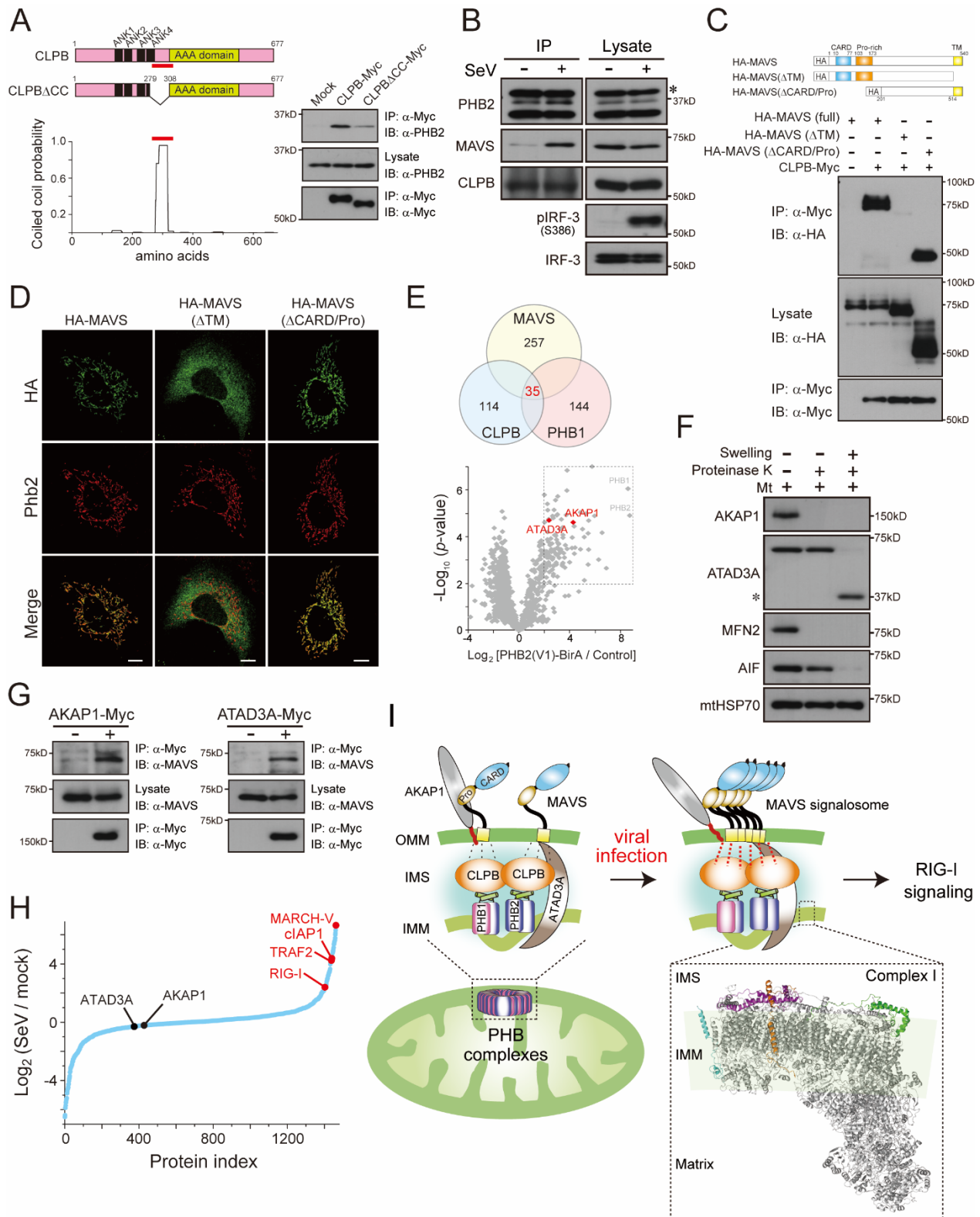(C) HEK293 cells stably expressing Myc-tagged CLPB were transfected with plasmids encoding HA-tagged MAVS variants, as indicated. Western blots of samples immunoprecipitated (IP) with the anti-Myc antibody or post-nuclear cell lysates (Lysate) were analyzed by immunoblotting (IB) with either the anti-HA monoclonal antibody HA.11 or the anti-Myc monoclonal antibody 9E10. The caspase recruitment domain (CARD), proline-rich domain (Pro-rich), and transmembrane segment (TM) in the MAVS structure are depicted (top cartoon), and the amino acid positions are indicated above the structure.

(D) The indicated HA-tagged MAVS variants in (C) were expressed in MEF cells, and their subcellular localizations were monitored by immunofluorescence against the HA antibody (green). Mitochondria in the same cells were identified by staining with an antibody against Phb2 (red). Scale bar, 10 μm.

(E) Identification of molecules that bridge the PHB complex to MAVS. Venn diagram in the top panel shows binding partners that overlapped (35 candidates) among the indicated molecules revealed by BioID2 assay (Table S5, abundance ratio > 7 for MAVS, and > 15 for both CLPB and PHB1). The volcano plot from Figure 1A is also shown at the bottom, and the positions of AKAP1 and ADAT3A are indicated in red.

(F) The mitochondrial fraction (Mt) isolated from HEK293 cells was treated with proteinase K (50 μg/mL) under regular (-) or hypotonic swelling (+) conditions for 15 min on ice. The reactants were developed by immunoblotting with antibodies against AKAP1, ATAD3A, or against several mitochondrial markers as indicated. OMM protein: MFN2. IMS protein: AIF. Matrix protein: mtHSP70. Asterisk indicates the C-terminal portion of ATAD3A.

(G) Interaction of endogenous MAVS with AKAP1 and ATAD3A. HEK293 cells were transfected with either AKAP1 (left) or ATAD3A (right) Myc-tagged encoding plasmids, and each lysate was subjected to immunoprecipitation (IP) with the anti-Myc antibody followed by Western blot analysis with anti-MAVS antibody.

(H) The interactions between AKAP1 and MAVS (also ATAD3A and MAVS) were not significantly altered during viral infection. A total of 1465 proteins identified from BioID2 experiments (BirA-MAVS ± SeV-infection) were plotted according to the abundance ratios (log_2) of SeV/mock against individual proteins (Protein index) sorted by their ratios in ascending order. Interactions, such as those of RIG-I and MAVS, were increased following the viral infection.

(I) Model of PHB complexes and their interactome that facilitates mitochondrial-mediated antiviral innate immunity. The PHB complexes localized in the IMM (left bottom) function in various mitochondrial homeostatic and cellular signaling processes. We propose that the PHB complexes comprising multi-oligomerizations of homotypic and/or heterotypic PHB dimers via their HR regions form an interactome assembly including CLPB, subunits of mitochondrial complex I, and other IMS proteins (left top, highlighted in blue background). Upon viral-infection, the PHB complexes associate with activated MAVS oligomers via CLPB with the assistance of proteins including AKAP1 and ATAD3A (middle), and the MAVS signalosome activates the RIG-I signaling pathway (right). These structural rearrangement events may be due to a functional role of CLPB, a molecular chaperone that responds to cellular stress. The right bottom inset shows the crystal structure of mitochondrial complex I (Zhu et al., 2016: PDB 5LC5), in which the specific subunits mentioned in the present study are colored in green (NDUFA8), cyan (NDUFB3), magenta (NDUFB10), and orange (NDUFB11).

Table S3, related to Figure 2. Crystallographic data and refinement statistics

Diffraction data

Resolution (last shell) (Å)	46.06-1.70 (1.73-1.70)
Space group	$P4_122$
Unit cell (Å)	65.14, 65.14, 62.29
Number of observed reflections	172,229 (6,789)
Number of unique reflections	15,289 (779)
Completeness (last shell) (%)	99.8 (99.0)
R_{merge} (%)	5.1 (41.8)
R_{meas} (last shell) (%)	5.5 (46.7)
$I/\sigma(I)$ (last shell)	22.3 (3.8)
$CC_{1/2}$ (%)	100.0 (93.0)

Refinement statistics

Resolution (Å)	46.06-1.70 (1.83-1.70)
R_{work} (%)	21.6 (34.1)
R_{free} (%)	23.9 (35.2)
r.m.s.d. bonds (Å)	0.008
r.m.s.d. angles (deg)	0.918
Average B factor (Å^2)	34.0
Number of atoms (Protein)	478
Number of atoms (Water)	75

Transparent Methods

Key Resources Table

REAGENT or RESOURCE	SOURCE	IDENTIFIER
Antibodies		
Mouse monoclonal anti-AIF (E-1)	Santa Cruz Biotechnology	sc-13116
Rabbit monoclonal anti-AKAP1 (D9C5)	Cell Signaling Technology	Cat# 5203
Mouse monoclonal anti-ATAD3A/B/C (A-4)	Santa Cruz Biotechnology	sc-376185
Rabbit polyclonal anti-ATAD3A (C-term)	Jacques Baudier Laboratory	Gilquin B. et al., 2010
Rabbit polyclonal anti-CLPB	Proteintech	15743-1-AP
Rabbit monoclonal anti-Cre recombinase (D3U7F)	Cell Signaling Technology	Cat# 12830
Rabbit monoclonal anti-CoxIV (3E11)	Cell Signaling Technology	Cat# 4850
Rabbit polyclonal anti-cytochrome *c* (H-104)	Santa Cruz Biotechnology	sc-7159
Rabbit polyclonal anti-HtrA2/Omi	R&D Systems	AF1458
Mouse monoclonal anti-HA epitope tag (HA.11)	Covance	MMS-101P
Rat monoclonal anti-mouse-IL-6	eBioscience	Cat# 14-7061-81
Rabbit polyclonal anti-IRF-3 (FL-425)	Santa Cruz Biotechnology	sc-9082
Rabbit monoclonal anti-IRF-3 (phospho S386)	Abcam	ab76493; EPR2346
Rabbit polyclonal anti-MAVS	Abcam	ab25084
Rabbit polyclonal anti-Mfn1 (H-65)	Santa Cruz Biotechnology	sc-50330
Rabbit polyclonal anti-Mic19/CHCHD3	Proteintech	25625-1-AP
Mouse monoclonal anti-mtHsp70	Thermo Fisher Scientific	MA3-028
Mouse monoclonal anti-*c*-Myc epitope tag (9E10)	Covance	MMS-150P
Mouse monoclonal anti-OPA1	BD Transduction Laboratories	Cat# 612606
Mouse monoclonal anti-PGK1 (22C5D8)	Thermo Fisher Scientific	Cat# 459250
Rabbit polyclonal anti-PHB2 (H-80)	Santa Cruz Biotechnology	sc-67045
Rabbit monoclonal anti-PHB2/REA	Abcam	ab181838; EPR14522
Rabbit monoclonal anti-PHB1	Abcam	ab75766; EPR2803Y
Mouse monoclonal anti-Tim23	BD Transduction Laboratories	Cat# 611223
Mouse monoclonal anti-Tom20 (F-10)	Santa Cruz Biotechnology	sc-17764
Rabbit polyclonal anti-Tom40	Santa Cruz Biotechnology	sc-11414
Alexa Fluor 488 goat anti-mouse IgG	Invitrogen	A-11001
Alexa Fluor 568 goat anti-rabbit IgG	Invitrogen	A-11011
Cy-3-conjugated sheep anti-mouse IgG	Jackson ImmunoResearch	Cat# 515-165-003
Bacterial and Virus Strains		

E. coli BL21(DE3) competent cells	Novagen	Cat# 69450-3
Sendai virus (Strain: Cantell)	ATCC	ATCC VR-907
Chemicals		
D-Biotin	Nacalai Tesque	Cat# 04822-04
Digitonin	Wako Pure Chemical Industries	Cat# 043-21371
Disuccinimidyl Dibutyric Urea (DSBU)	Thermo Fisher Scientific	Cat# A35459
3,3'-Diaminobenzidine	Tokyo Chemical Industry	D3756
Isopropyl β-D-1-thiogalactopyranoside (IPTG)	Nacalai Tesque	Cat# 19742-94
Lipofectamine 2000	Thermo Fisher Scientific	Cat# 11668019
Lipofectamine RNAiMAX	Thermo Fisher Scientific	Cat# 13778150
Protease inhibitor cocktail	Roche	Cat# 11 836 153 001
Phenylmethylsulfonyl fluoride (PMSF)	Nacalai Tesque	Cat# 06297-02
poly(I:C)	InvivoGen	Cat# tlrl-pic
TRIzol	Invitrogen	Cat# 15596026
Reverse Transcriptase (M-MLV)	Wako Pure Chemical Industries	Cat# 187-01281
PrimeSTAR HS DNA Polymerase	Takara Bio	R010A
D-MEM, high glucose	Gibco	Cat# 11965092
Bovine calf serum (BCS)	Gibco	Cat# 160170-078
Fetal bovine serum (FBS)	Gibco	Cat# 10437028
Penicillin-Streptomycin	Gibco	Cat# 15140122
GlutaMAX	Gibco	Cat# 35050061
Puromycin	Sigma-Aldrich	P8833
Blasticidin	InvivoGen	Cat# ant-bl-05
Hygromycin B	Sigma-Aldrich	H3274
G-418 (Geneticin)	Roche	Cat# 04 727 878 001
MitoTracker Red CMXRos	Invitrogen	M7512
Anti-c-Myc Agarose beads	Sigma-Aldrich	A7470
Streptavidin Agarose beads	Sigma-Aldrich	S1638
Protein A Sepharose beads	Sigma-Aldrich	P3391
Nickel-nitriotriacetate (Ni-NTA) agarose	QIAGEN	Cat# 30210
HiTrap Q HP	GE Healthcare	Cat# 17115301
Critical Commercial Assays		
Human IFN-β ELISA Kit	Kamakura Techno-Science	Cat# KTS301

Mouse IFN-β ELISA Kit	R&D Systems	Cat# 42400-1
Dual-Luciferase reporter assay system	Promega	E1910
Deposited Data		
PHB2[188-265] crystal structure	This paper	PDB: 6IQE
BioID2 data [Control, PHB2(V1), PHB2(V3)]	This paper	jPOST: PXD011939
BioID2 data (PHB2[WT], PHB2[I225P], PHB2[KKK])	This paper	jPOST: PXD011946
BioID2 data (MAVS, CLPB, PHB1)	This paper	jPOST: PXD014218
Cross-linking MS data	This paper	jPOST: PXD011941 and PXD014217
Experimental Models: Cell Lines		
HEK293	Tsurimoto Laboratory	N/A
A549	Ichinohe Laboratory	N/A
HeLa	Mihara Laboratory	N/A
Phb2[flox/flox] MEFs	Thomas Langer Laboratory	N/A
Platinum-A retroviral packaging cell line	Cell Biolabs	RV-102
Experimental Models: Yeast strains		
Wild Type (TKY705) (genetic background W303): *MAT*a *ura3-52 trp1Δ leu2-3_112 his3-11 ade2-1*	Miyata N. et al., 2017	N/A
Wild Type (TKY706) (genetic background W303): *MAT*α *ura3-52 trp1Δ leu2-3_112 his3-11 ade2-1 can1 Δ ::STE2pr-Sp_his5*	Miyata N. et al., 2017	N/A
*psd*1Δ (TKY707): TKY705, *psd1Δ::kanMX4*	Miyata N. et al., 2017	N/A
phb1Δ (OKY7207): TKY706, *phb1Δ::hphNT1*	This paper	N/A
PSD1/psd1Δ PHB1/phb1Δ (OKY7208) (genetic background W303): *MAT*a/α *ura3-52/ura3-52 trp1Δ/ trp1Δ leu2-3_112/ leu2-3_112 his3-11/his3-11 ade2-1/ade2-1 CAN1/can1 Δ ::STE2pr-Sp_his5 PSD1/psd1Δ::kanMX4 PHB1/phb1 Δ::hphNT1*	This paper	N/A
Oligonucleotides		
Human PHB2 (A.A.1) forward (TK1090): 5'-aaagctagcgtttaaaccatggcccagaacttgaaggacttgg	FASMAC	N/A
Human PHB2 (A.A.299) reverse (TK1091): 5'-tttgaattctttcttacccttgatgaggc	FASMAC	N/A
Human PHB2 (A.A.188) forward (TK1028): 5'-tttaccatgggggagctttagccgagagtacacagc-3'	FASMAC	N/A
Human PHB2 (A.A.247) reverse (TK1029): 5'-tttctcgaggccagggttcttgctcagtgc-3'	FASMAC	N/A
Human PHB2 (I225P) mutation forward: 5'-cggcagaaaCCtgtgcaggccgag-3'	FASMAC	N/A
Human PHB2 (I225P) mutation reverse: 5'-ctcggcctgcacaGGtttctgccg-3'	FASMAC	N/A
Human PHB2 (KKK) mutation forward: 5'-gcaggccAagggtAaggccAaggctgcc-3'	FASMAC	N/A

Human PHB2 (KKK) mutation reverse: 5'-ggcagcctTggcctTaccctTggcctgc-3'	FASMAC	N/A
Human CLPB (A.A.1) forward: 5'-aaagctagcaccatgctggggtccctggtgttgaggagaaaagc-3'	FASMAC	N/A
Human CLPB (A.A.677) reverse: 5'-tttggtaccgatggtgttgcacaccttctcagggtgcagtgg-3'	FASMAC	N/A
Human CLPB (Δ A.A.280-307) deletion forward: 5'-ggattatgcccgagaagggccctggagcagcgactaaagg-3'	FASMAC	N/A
Human CLPB (Δ A.A.280-307) deletion reverse: 5'-cctttagtcgctgctccaggggccttctcgggcataatcc-3'	FASMAC	N/A
Human AKAP1 (A.A. 1) forward: 5'-aaagcggccgcaccatggcaatccagttccgttcgctcttcccc-3'	FASMAC	N/A
Human AKAP1 (A.A. 903) reverse: 5'-tttggtaccaaggcttgtgtagtagctgtctacccactgg-3'	FASMAC	N/A
Human ATAD3A (A.A. 1) forward: 5'-aaagctagcaccatgtcgtggctcttcggcattaacaagggc-3'	FASMAC	N/A
Human ATAD3A (A.A. 634) reverse: 5'-tttggtaccggatggggagggctcgtccccacgc-3'	FASMAC	N/A
S. cerevisiae genomic DNA (*Phb1* ORF) forward: 5'-aaactcgagggtaggggttcgctatggggtcatcactggcc-3'	FASMAC	N/A
S. cerevisiae genomic DNA (*Phb1* ORF) reverse: 5'-tttggatccgcagccaccgctttggctgtaggtataagatgcc-3'	FASMAC	N/A
S. cerevisiae Phb1-Myc tag (A.A. 287) forward: 5'-agtggagaacaaaagttgatttctgaagaagatttgtaagtctggaaa agctatgaacacaataaactag-3'	FASMAC	N/A
S. cerevisiae Phb1-Myc tag (A.A. 287) reverse: 5'-ttacaaatcttcttcagaaatcaacttttgttctccactacggccaatgtt caaaagcaaggaatttgg-3'	FASMAC	N/A
S. cerevisiae Phb1 (V202P) mutation forward: 5'-gccaaattccttCCcgaaaaggcagagc-3'	FASMAC	N/A
S. cerevisiae Phb1 (V202P) mutation reverse: 5'-gctctgcctttcgGGaaggaatttggc-3'	FASMAC	N/A
S. cerevisiae Phb1 (V213P) mutation forward: 5'-gagacaagcttctCCtatcagagctgaagg-3'	FASMAC	N/A
S. cerevisiae Phb1 (V213P) mutation reverse: 5'-ccttcagctctgataGGagaagcttgtctc-3'	FASMAC	N/A
S. cerevisiae Phb1 (KKK) mutation forward: 5'-gttatcagagctAaaggtAaagcaAaaagtgctgaattc-3'	FASMAC	N/A
S. cerevisiae Phb1 (KKK) mutation reverse: 5'-gaattcagcactttTtgcttTacctttAgctctgataac-3'	FASMAC	N/A
S. cerevisiae Phb1 disruption forward: 5'-acgaaacttacattcaaaatcaataatttactttagaaaagaatgcgta tgcaggtcgac-3'	Sigma-Aldrich	N/A
S. cerevisiae Phb1 disruption reverse: 5'-aattttctcccctagtttattgtgttcatagctttccagacttaatcgatg aattcgagctcg-3'	Sigma-Aldrich	N/A
siRNA		
AKAP1 Sense siRNA sequence *UCAACAUCAUGUAGACAAAtt*	Thermo Fisher Scientific	s15665
ATAD3A Sense siRNA sequence *UGGUGAGAAUGUAUUUUGAtt*	Thermo Fisher Scientific	s30448
CCDC58 Sense siRNA sequence #1 *AGUCUUUGAUGGCAGCUCAtt*	Thermo Fisher Scientific	s228144

CCDC58 Sense siRNA sequence #2 *AGAACUGAAUGUUGAAGAAtt*	Thermo Fisher Scientific	s43575
CCDC58 Sense siRNA sequence #3 *CAGACAAAGUUGAAAUGGAtt*	Thermo Fisher Scientific	s43576
CMC2 Sense siRNA sequence #1 *GGUUGAUACCUGAAAGAAUtt*	Thermo Fisher Scientific	s226898
CMC2 Sense siRNA sequence #2 *GCAUUGCAAUGCGAAAGAAtt*	Thermo Fisher Scientific	s32444
CMC2 Sense siRNA sequence #3 *GAUCGGGAGUUGAGAAAAUtt*	Thermo Fisher Scientific	s32446
DIABLO Sense siRNA sequence #1 *GACUGCAGUUGGUCUUUCAtt*	Thermo Fisher Scientific	s32189
DIABLO Sense siRNA sequence #2 *CCGACAAUAUACAAGUUUAtt*	Thermo Fisher Scientific	s32187
DIABLO Sense siRNA sequence #3 *UCUCUUUACCGACAAUAUAtt*	Thermo Fisher Scientific	s32188
PGAM5 Sense siRNA sequence #1 *AGCUGUGCAGUAUUACGAAtt*	Thermo Fisher Scientific	s46938
PGAM5 Sense siRNA sequence #2 *GCAGUAUUACGAAGACGGAtt*	Thermo Fisher Scientific	s46937
PGAM5 Sense siRNA sequence #3 *CCAGGCGUCUGCAAAGUCAtt*	Thermo Fisher Scientific	s195818
NDUFB11 Sense siRNA sequence #1 *GCGACUUGUCUUCUUCUUUtt*	Thermo Fisher Scientific	s224300
NDUFB11 Sense siRNA sequence #2 *CGUGGGAUGGGAUGAAAGAtt*	Thermo Fisher Scientific	s29163
NDUFB11 Sense siRNA sequence #3 *CCGAGGACGAAAACUUGUAtt*	Thermo Fisher Scientific	s29165
CLPB Sense siRNA sequence #1 *GGAUCAUCUGGAAUAGGAAtt*	Thermo Fisher Scientific	s224882
CLPB Sense siRNA sequence #2 *GGAAGACCAUUGAUUGCAAtt*	Thermo Fisher Scientific	s37653
CLPB Sense siRNA sequence #3 *GCUUUGGAGAUGAGCCGUAtt*	Thermo Fisher Scientific	s37655
NDUFB3 Sense siRNA sequence #1 *CUGCAUUUGUGGUAGCUGUtt*	Thermo Fisher Scientific	s9355
NDUFB3 Sense siRNA sequence #2 *ACUUCCAGAUUAUAGACAAtt*	Thermo Fisher Scientific	s9356
NDUFB3 Sense siRNA sequence #3 *AGAUAGAAGGGACACCAUUtt*	Thermo Fisher Scientific	s9357
CKMT1B Sense siRNA sequence #1 *GCACACCACGGAUCUAGAUtt*	Thermo Fisher Scientific	s3097
CKMT1B Sense siRNA sequence #2 *AGGUAUGUAUUGUCCUCUAtt*	Thermo Fisher Scientific	s3099
CKMT1B Sense siRNA sequence #3 *GUAUUGUCCUCUAGAGUCAtt*	Thermo Fisher Scientific	s3098
NDUFA8 Sense siRNA sequence #1 *GCAGUUAUUUCGUCACUGUtt*	Thermo Fisher Scientific	s9342
NDUFA8 Sense siRNA sequence #2 *GGAGAACUGUCAAAGGUCAtt*	Thermo Fisher Scientific	s9340
NDUFA8 Sense siRNA sequence #3 *GGACUUCUUUAGGCAGAUAtt*	Thermo Fisher Scientific	s9341

IMMP2L Sense siRNA sequence #1 *AGAGAGUGAUUGCUCUUGAtt*	Thermo Fisher Scientific	s38358
IMMP2L Sense siRNA sequence #2 *GGGUUGAAGGUGAUCAUCAtt*	Thermo Fisher Scientific	s38357
IMMP2L Sense siRNA sequence #3 *GUGGUGACAUUGUAUCAUUtt*	Thermo Fisher Scientific	s38356
NDUFB10 Sense siRNA sequence #1 *GGACUACAAAGUCGACCAAtt*	Thermo Fisher Scientific	s9375
NDUFB10 Sense siRNA sequence #2 *GUGCAUGUAUGAAGCCGAAtt*	Thermo Fisher Scientific	s9376
NDUFB10 Sense siRNA sequence #3 *GCAGAACUGUAUCAAGGAAtt*	Thermo Fisher Scientific	s9374
PHB1 Sense siRNA sequence #1 *UCACAACUGAGAUCCUCAAtt*	Thermo Fisher Scientific	s10426
PHB1 Sense siRNA sequence #2 *CGUGGGUACAGAAACCAAUtt*	Thermo Fisher Scientific	s10424
PHB1 Sense siRNA sequence #3 *GCAUCGGAGAGGACUAUGAtt*	Thermo Fisher Scientific	s10425
Silencer Select Negative Control No. 1 *siRNA*	Thermo Fisher Scientific	Cat# 4390843
Recombinant DNA		
Plasmid: pET28a/PHB2$^{188\text{-}247}$-6×His	This study	N/A
Plasmid: pET28a/PHB2$^{188\text{-}247}$(I225P)-6×His	This study	N/A
Plasmid: pET28a/PHB2$^{188\text{-}247}$(KKK)-6×His	This study	N/A
Plasmid: pET28a/PHB2$^{188\text{-}265}$-6×His	This study	N/A
Plasmid: pcDNA3.1(-)/C terminal-3×Myc tag	Yasukawa K. et al., 2009	N/A
Plasmid: pcDNA3.1(-)/PHB2-3×Myc	This study	N/A
Plasmid: pcDNA3.1(-)/PHB2^{I225P}-3×Myc	This study	N/A
Plasmid: pcDNA3.1(-)/PHB2^{KKK}-3×Myc	This study	N/A
Plasmid: pcDNA3.1(-)/CLPB-3×Myc	This study	N/A
Plasmid: pcDNA3.1(-)/CLPB$^{\Delta280\text{-}307}$-3×Myc	This study	N/A
Plasmid: pcDNA3.1(-)/AKAP1-3×Myc	This study	N/A
Plasmid: pcDNA3.1/ATAD3A-myc-6×His	Gilquin B. et al., 2010	N/A
Plasmid: MCS-BioID2-HA	Addgene (Kyle Roux Lab)	Cat# 74224
Plasmid: pcDNA3.1/PHB2(V1)-BirA-HA	This study	N/A
Plasmid: pcDNA3.1/PHB2(V3)-BirA-HA	This study	N/A
Plasmid: pcDNA3.1/PHB2^{I225P}-BirA-HA	This study	N/A
Plasmid: pcDNA3.1/PHB2^{KKK}-BirA-HA	This study	N/A
Plasmid: pcDNA3.1/PHB1-BirA-HA	This study	N/A
Plasmid: pcDNA3.1/CLPB-BirA-HA	This study	N/A

Plasmid: pMXs-puro	Cell Biolabs	RTV-012
Plasmid: pMXs-puro/PHB2-3×Myc	This study	N/A
Plasmid: pMXs-puro/PHB2^{I225P}-3×Myc	This study	N/A
Plasmid: pMXs-puro/PHB2^{KKK}-3×Myc	This study	N/A
Plasmid: pMXs-puro/PHB2(V1)-BirA-HA	This study	N/A
Plasmid: pMXs-puro/PHB2(V3)-BirA-HA	This study	N/A
Plasmid: pMXs-puro/NLS-Cre	This study	N/A
Plasmid: pMXs-puro/NLS-Cre-eGFP	This study	N/A
Plasmid: pMXs-puro/CLPB-3×Myc	This study	N/A
Plasmid: myc-BioID2-MCS	Addgene (Kyle Roux Lab)	Cat# 74223
Plasmid: pcDNA3.1/myc-BirA-MAVS$^{1-540}$	This study	N/A
Plasmid: pcDNA3.1(-)/3×Myc-MAVS$^{1-540}$	Yasukawa K. et al., 2009	N/A
Plasmid: pcDNA3.1(-)/3×HA-MAVS$^{1-540}$	Yasukawa K. et al., 2009	N/A
Plasmid: pcDNA3.1(-)/3×HA-MAVS$^{1-514}$	Yasukawa K. et al., 2009	N/A
Plasmid: pcDNA3.1(-)/3×HA-MAVS$^{201-540}$	Yasukawa K. et al., 2009	N/A
Plasmid: pcDNA3.1(-)/RIG-I$^{1-250}$-7×Myc	Yasukawa K. et al., 2009	N/A
Plasmid: pRS416	ATCC	ATCC 87521
Plasmid: pRS416/yPhb1^{WT}-Myc	This study	N/A
Plasmid: pRS416/yPhb1^{V202P}-Myc	This study	N/A
Plasmid: pRS416/yPhb1^{V213P}-Myc	This study	N/A
Plasmid: pRS416/yPhb1$^{V202/213P}$-Myc	This study	N/A
Plasmid: pRS416/yPhb1^{KKK}-Myc	This study	N/A
Software and Algorithms		
COILS	Lupas A. et al., 1991	https://embnet.vital-it.ch/software/COILS_form.html
GraphPad QuickCalcs	GraphPad Software	https://www.graphpad.com/quickcalcs/ttest1.cfm
PyMOL version 2.1.1	The PyMOL Molecular Graphics System, Version 2.0 Schrödinger, LLC	https://pymol.org/2
Proteome Discoverer version 2.2	Thermo Fisher Scientific	OPTON-30795
CCP4 6.4.0	Winn M.D. et al., 2011	http://www.ccp4.ac.uk/index.php

Xds version May 1, 2016	Kabsch W., 2010	http://xds.mpimf-heidelberg.mpg.de/
Phenix version 1.8.4-1496	Adams P.D. et al., 2010	https://www.phenix-online.org/
Coot 0.7.2	Emsley P. et al., 2010	https://www2.mrc-lmb.cam.ac.uk/personal/pemsley/coot/

Cell lines and virus

HEK293 cells (obtained from the Tsurimoto Laboratory, species: human, sex: female) were maintained in Dulbecco's modified Eagle medium (D-MEM) (high glucose; 4,500 mg/L) supplemented with 1% GlutaMAX, penicillin (100 U/mL)-streptomycin (100 μg/mL), and 10% bovine calf serum (BCS) at 5% CO_2 and 37° C. A549 (obtained from the Ichinohe Laboratory, species: human, sex: male), HeLa (obtained from the Mihara Laboratory, species: human, sex: female), and *Phb2^flox/flox* MEFs (obtained from the Langer Laboratory, species: mouse, sex: unknown) were maintained in D-MEM medium supplemented with 1% GlutaMAX, penicillin (100 U/mL)-streptomycin (100 μg/mL), and 10% fetal bovine serum (FBS) at 5% CO_2 and 37° C. The Platinum-A retroviral packaging cell line (obtained from Cell Biolabs: human, sex: unknown) was similarly maintained in D-MEM/FBS medium, except with the addition of puromycin (1 μg/mL) and blasticidin (10 μg/mL). Cells used in the study were authenticated via a Short Tandem Repeat analysis. Sendai virus Cantell strain used in the study was purchased from the American Type Culture Collection (ATCC).

Yeast strains and their genotyping

The yeast strains were grown in YPAD medium (pH 6.0) containing 1% yeast extract, 2% peptone, 0.008% adenine, and 2% glucose. Synthetic complete medium plus adenine (SCAD medium, pH 6.0) containing 0.67% yeast nitrogen base without amino acids, 0.2% drop-out mix, 0.008% adenine, and 2% glucose without uracil was used for selecting the uracil-prototrophic transformants. SCAD-MSG medium (pH 6.0) containing 0.17% yeast nitrogen base without amino acids and ammonium sulfate, 0.1% *L*-glutamic acid sodium salt, 0.2% drop-out mix, 0.008% adenine, and 2% glucose, without histidine and uracil was used for random spore analyses (Tong and Boone, 2006). Complete disruption of the *phb1* gene was accomplished by polymerase chain reaction (PCR)-based gene replacement (Lorenz et al., 1995) using a hygromycin-resitant cassette amplified from a plasmid pFA6a-hphNT1 (Janke et al., 2004) with a pair of gene-specific primers (PHB1 disruption forward/reverse oligonucleotides in the Key Resources Table). A diploid yeast strain, *PSD1/psd1Δ PHB1/phb1Δ* (OKY7208), was obtained by mating a *MATa* strain, *psd1Δ::kanMX4* and a *MATα* strain, *phb1Δ::hphNT1*, followed by incubation on a diploid selection agar-plate containing YPD medium supplemented with 200 μg/mL of G-418 and 300 μg/mL of hygromycin B.

Plasmids

To construct human PHB2 (variants 1 and 3) plasmids used in the BioID2 study, HEK293 cDNA was used as a template for PCR to amplify the gene. Using the oligonucleotides TK1090 and TK1091, each amplified fragment containing 5' *Nhe*I and 3' *EcoR*I sites was subcloned into a plasmid (MCS-BioID2-HA; Addgene #74224) containing a carboxyl-terminal HA epitope tag with a biotin ligase from *Aquifex aeolicus*. To generate PHB2 bacterial expression constructs, the plasmid pcDNA3.1/PHB2(V1)-BirA-HA was used as a template to PCR-amplify regions encoding residues 188–247 (coiled-coil motif) with a forward primer (TK1028) containing a 5' *Nco*I restriction site and a reverse primer (TK1029) containing a 3' *Xho*I site. The amplified fragment was ligated into pET28a (+) (Novagen), which contains a C-terminal 6×His tag. The human CLPB, AKAP1, and ATAD3A-encoding genes were obtained from HEK293 cells, and the cDNAs were each subcloned into a pcDNA3.1(-)/3×Myc vector in-frame with 3×Myc tag (Yasukawa et al., 2009). To construct pRS416/yPhb1-Myc, a yeast centromere plasmid carrying *Phb1*, a genomic fragment containing the *Phb1*-coding region with 500 bp of the 5′ and 3′ flanking sequences was amplified by PCR from the *S. cerevisiae* genomic DNA of *MATα* strain using primer sets of *Phb1 ORF* forward and reverse, and then cloned into pRS416 (ATCC 87521) in-frame with a Myc epitope tag. Mutations of each plasmid used in the study were introduced by overlap PCR mutagenesis and confirmed by DNA sequencing (ABI 3100). To generate retroviral expression constructs, each cDNA was subcloned into the retroviral vector pMXs-puro (Cell Biolabs). The retroviral expression vectors were then transfected into platinum packaging cell lines by calcium phosphate precipitation, and the retroviral supernatants were harvested 48 h post-transfection and used to infect cells. The plasmid encoding Cre recombinase fused with a nuclear localization signal (NLS) was obtained from Addgene (#13763).

Protein expression and purification

PHB2$^{188-247}$ (or PHB2$^{188-265}$) with a C-terminal 6×His tag and its variants were expressed in *E. coli* BL21(DE3) cells. Inoculated cultures were grown to log phase at 37º C. Overproduction of recombinant protein was induced by the addition of isopropyl β-D-1-thiogalactopyranoside to a final concentration of 1 mM at 15º C for overnight induction. The next day, cells were collected by centrifugation (6,700g for 15 min), and the pellets were stored frozen (-20° C) until purification. Bacterial pellets were resuspended in 50 mM Tris-buffered saline (pH 8.0) containing 300 mM NaCl, 10% glycerol (w/v), 15 mM imidazole, and 1 mM phenylmethylsulfonyl fluoride (PMSF), lysed by sonication, and centrifuged at 18,800g at 4º C for 15 min to obtain a soluble fraction. After clarification, the histidine-tagged

proteins were affinity-purified on nickel-nitriotriacetate (Ni-NTA) agarose columns at 4° C. Proteins bound to the beads were eluted with 50 mM Tris-HCl buffer (pH 8.0) containing 300 mM NaCl and 100 mM imidazole.   After elution, all proteins were purified to >95% purity by anion exchange chromatography using a HiTrapQ column equilibrated with 50 mM Tris-HCl buffer (pH 8.5).   Protein concentrations were determined by absorbance at 280 nm in 6M guanidine hydrochloride (Edelhoch 1967).

Circular dichroism spectroscopy

CD measurements were performed in 1× phosphate-buffer saline (PBS; pH 7.4) with a Jasco J-715 spectropolarimeter (JASCO Co).   Wavelength scans (200 to 250 nm) were performed on 10 μM protein solutions using a cell with 0.2 cm optical path length at 4° C.

Crystallization, X-ray data collection, and structure determination

Crystallizations were performed using the histidine-tagged PHB2[188-265] protein. Diffraction-quality crystals of PHB2[188-265] were obtained by vapor diffusion of hanging drops at 20° C by equilibrating protein against a reservoir solution containing 1.0 M ammonium chloride and 0.1 M sodium acetate (pH 4.5).   Bipyramidal crystals belonged to the space group $P4_122$ ($a = b = 65.14$ Å, $c = 62.29$ Å).   Crystals were soaked into a cryoprotectant solution containing 1.1 M ammonium chloride, 0.1 M sodium acetate (pH 4.5), and 20% (w/v) glycerol, and flash-frozen in liquid nitrogen for synchrotron data collection.

The X-ray diffraction data of the PHB2[188-265] crystals were collected from a single crystal at 100K on a PILATUS 6M pixel detector (Dectris) using a single wavelength (1.0000 Å) at beamline BL41XU at SPring-8, Japan.   Integrated intensities were obtained with the program XDS and scaled using the program AIMLESS in the CCP4 package.   The initial model of the PHB2[188-265] was obtained by molecular replacement using the program PHASER.   The search model was a monomer in a computationally designed three-helix bundle (PDB ID: 4TQL). Structural refinement was performed using phenix.refine from the PHENIX suite.   In the final refined structure, only residues 188-245 were ordered.   The crystal structure contained 76 water molecules.   The refined coordinate for PHB2[188-265] was deposited in the Protein Data Bank (PDB ID: 6IQE).   Data processing and crystallographic refinement statistics are summarized in Table S3.

Mitochondrial fractionation and proteolysis

Mitochondrial fractionation, proteolysis and membrane association assays were performed as previously described (Yoshizumi et al. 2014) with slight modifications.   Briefly, cultured cells were washed once with 1× PBS (pH 7.4), scraped off the culture plate, and lysed in

homogenization buffer containing 20 mM HEPES (pH 7.5), 70 mM sucrose, and 220 mM mannitol by 30 strokes in a Dounce homogenizer. The homogenate was then centrifuged at 800*g* for 5 min (4° C) to precipitate the nuclei, and the resulting supernatant was further centrifuged at 10,000*g* for 10 min (4° C) to precipitate the crude mitochondrial fraction.

For the proteinase K resistance assay, the isolated mitochondria pellet was resuspended in either the homogenization buffer or a hypotonic buffer [20 mM HEPES (pH 7.5)] and maintained on ice for 30 min to cause swelling. The samples were then treated with proteinase K (50 μg/mL) for 15 min (on ice), and reactants were subjected to Western blot analysis with the indicated antibodies.

Blue-Native PAGE

The isolated mitochondrial fraction was lysed in a BN-PAGE lysis buffer containing 20 mM Bis-Tris (pH 7.0), 2 mM NaCl, 500 mM aminocaproic acid, 1 mM EDTA, 10% (v/v) glycerol, 0.5% (w/v) digitonin, and protease inhibitor cocktail on ice for 15 min. The clarified supernatant was supplemented with 0.5% (w/v) Coomassie brilliant blue G-250, separated on 4-12% BN-PAGE, and immunoblotted with the indicated antibodies.

The proximity-dependent biotin identification (BioID2)

The proximity-dependent biotin identification (BioID2) method was performed as previously described (Kim et al. 2016) with slight modifications. Briefly, confluent HEK293 cells in 10-cm dish that stably expressed PHB2(V1 or V3) or other proteins fused at the C-terminus with the biotin ligase from *A. aeolicus* were incubated with 100 μM biotin for 18 h. After washing once with 1× PBS (pH 7.4), the cells were scraped off and mitochondria from the cells were isolated as described above. The mitochondrial fractions were then washed once with the homogenization buffer and lysed in 800 μL radio immunoprecipitation assay (RIPA) buffer containing 50 mM Tris-HCl (pH 7.4), 150 mM NaCl, 1 mM EDTA-EGTA, 10% (w/v) glycerol, 1% (w/v) Nonidet P-40 (NP-40), 0.1% sodium dodecyl sulfate (SDS), and 0.1% sodium deoxycholate for 1 h at 4° C. The clarified supernatants were incubated with 20 μL of streptavidin agarose beads for 2 h at 4° C, followed by washing three times with RIPA buffer and twice with 50 mM ammonium bicarbonate. Proteins on the beads were digested by adding 200 ng trypsin/Lys-C mix (Promega) for 16 h at 37° C. The digests were desalted using GL-Tip SDB (GL Sciences), and the eluates were evaporated in a SpeedVac concentrator (Thermo Fisher Scientific).

LC-MS/MS analysis of the resultant peptides was performed on an EASY-nLC 1200 UHPLC connected to a Q Exactive Plus mass spectrometer through a nanoelectrospray ion source (Thermo Fisher Scientific). The peptides were separated on a 75-μm inner diameter × 150 mm

C18 reverse-phase column (Nikkyo Technos) with a linear gradient from 4%-28% acetonitrile for 0-150 min followed by an increase to 80% acetonitrile during 150-170 min. The mass spectrometer was operated in a data-dependent acquisition mode with a top 10 MS/MS method. MS1 spectra were measured with a resolution of 70,000, an AGC target of 1×10^6, and a mass range from 350 to 1,500 m/z. HCD MS/MS spectra were acquired at a resolution of 17,500, an AGC target of 5×10^4, an isolation window of 2.0 m/z, a maximum injection time of 60 ms, and a normalized collision energy of 27. Dynamic exclusion was set to 10 s. Raw data were directly analyzed against the SwissProt database restricted to *Homo sapiens* using Proteome Discoverer version 2.2 (Thermo Fisher Scientific) for identification and label-free precursor ion quantification. The search parameters were as follows: (a) trypsin as an enzyme with up to two missed cleavages; (b) precursor mass tolerance of 10 ppm; (c) fragment mass tolerance of 0.02 Da; and (d) acetylation of protein N-terminus, oxidation of methionine, and deamidation of asparagine and glutamine as variable modifications. Peptides were filtered at a false-discovery rate of 1% using the percolator node. Normalization was performed such that the total sum of abundance values for each sample over all peptides was the same. The MS proteomics data of BioID2 were deposited to the ProteomeXchange Consortium via the jPOST partner repository (https://repository.jpostdb.org) with the dataset identifiers JPST000527/PXD011939, JPST000529/PXD011946, and JPST000618/PXD014218 (Okuda et al., 2017).

Cross-linking mass spectrometry

In a 10-cm dish, mitochondria were isolated from confluent HEK293 cells stably expressing PHB2(V1) or PHB1 with a C-terminal 3×Myc tag, and resuspended in a cross-linking buffer [1× PBS (pH 7.4) and 50 or 100 μM DSBU (Thermo Fisher Scientific)] for 30 min at room temperature. After the cross-linking reaction, the resultant proteins were incubated with 50 mM Tris-HCl (pH 7.5) for 15 min at room temperature to quench the excess DSBU. The cross-linked mitochondria were then lysed in 600 μL of RIPA buffer for 1 h at 4° C, followed by centrifugation at 15,000 g for 10 min. The clarified supernatants were incubated with 20 μL of anti *c*-Myc agarose beads, followed by washing three times with 1× PBS (pH 7.4) and twice with 50 mM ammonium bicarbonate. Proteins on the beads were digested by adding 400 ng trypsin/Lys-C mix for 16 h at 37° C. The digests were desalted using GL-Tip SDB, and the eluates were evaporated in a SpeedVac concentrator.

The resultant peptides were divided into two halves and subjected to LC-MS/MS analysis using both Q Exactive Plus and Orbitrap Fusion Lumos mass spectrometers with the EASY-nLC 1200 systems. Raw data were analyzed using Proteome Discoverer version 2.2 with the XlinkX node (Liu et al., 2017) to identify cross-linked peptides. The MS proteomics data of cross-linking MS were deposited to the ProteomeXchange Consortium via the jPOST

partner repository with the dataset identifier JPST000528/PXD011941 and JPST000617/PXD014217.

Confocal microscopy

Cells were plated on coverslips in 12-well plates (5×10^4 cells/well).   The following day, the cells were fixed with 4% paraformaldehyde for 10 min, permeabilized with 0.2% Triton X-100 in 1× PBS (pH 7.4), and blocked with 5% BCS.   Epitope tagged PHB2 proteins (HA- or Myc-) were detected with its specific polyclonal primary and AlexaFluor488 secondary antibodies, and mitochondria were stained with anti-mtHSP70 primary antibody followed by the Cy3-conjugated secondary antibody.   In some experiments, cells were incubated with 150 nM MitoTracker Red CMXRos for 1 h before fixation and then followed the same process described above (monitoring the $\Delta\Psi_m$).   Cells were imaged with a C2$^+$ confocal microscope (Nikon Instruments Inc).

Electron microscopy

For electron microscopy, cells were fixed in 100 mM cacodylate buffer (pH 7.4) containing 2% paraformaldehyde and 2% glutaraldehyde for 1 h, washed and fixed again with 100 mM cacodylate buffer containing 2% glutaraldehyde overnight at 4° C.   After fixation, the cells were washed 4 times with 100 mM cacodylate buffer for 20 min each, and post-fixed with 2% osmium tetroxide (OsO$_4$) in cacodylate buffer at 4° C for 1 h.   Cells were then dehydrated in a graded series of ethanol (50%, 70%, 90%, and 100%), embedded in resin (Quetol 812, Nisshin EM Co, Japan), and polymerized at 60° C for 48 h.   The polymerized resins were cut in ultra-thin sections at 70 nm with an LEICA UTC ultramicrotome, mounted on copper grids, and stained with 2% uranyl acetate and lead solution (Sigma-Aldrich).   Images were collected with a transmission electron microscope (JEM-1400Plus; JEOL Ltd, Japan) operating at 80 kV and equipped with a CCD camera (VELETA; Olympus Soft Imaging Solutions GmbH, Germany).

RNA interference

For RNA interference knockdown experiments, 21-nucleotide siRNAs were purchased from Thermo Fisher Scientific (Silencer Select Custom siRNA Library).   HEK293 (or A549/HeLa) cells were each transfected with 10 nM siRNA (final concentration) three times within 48 h using Lipofectamine RNAiMAX (Thermo Fisher Scientific) following the manufacturer's protocols.   At 72 h after the initial treatment, the siRNA-treated cells were used for some functional assays.   Silencer Select Negative Control No. 1 siRNA was used as the control.

Dual luciferase reporter assay

HEK293 cells (3×10^5 cells/well) pre-treated with siRNAs were plated in 24-well plates. The following day, cells were co-transfected with 100 ng of a luciferase reporter plasmid p125luc, 2.5 ng of the Renilla luciferase internal control vector phRL-TK (Promega), and each of the indicated expression plasmids using Lipofectamine 2000 reagent (Thermo Fisher Scientific) following the manufacturer's protocols. Empty vector [pcDNA3.1(-)] (Invitrogen) was used to maintain equivalent amounts of DNA in each well. Cells were harvested 24 h post-transfection, and analyzed by a dual-luciferase reporter assay on the GloMax 20/20n luminometer (Promega). Each experiment was replicated at least three times.

ELISA

Production of IFN-β was measured with species-specific enzyme-linked immunosorbent assay (ELISA) reagents for human and murine IFN-β from Kamakura Techno-Science Inc. and R&D Systems, respectively. Murine IL-6 was measured using its specific antibody from eBioscience.

Immunoprecipitation

For co-immunoprecipitation experiment, HEK293 cells at 80% confluence were transiently transfected with the appropriate plasmids (2 μg each) in a six-well plate by the calcium phosphate method. Two days after transfection, cells were lysed with 1 mL lysis buffer containing 50 mM Tris-HCl (pH 7.4), 150 mM NaCl, 10% (w/v) glycerol, 1% NP-40, and protease inhibitor cocktail and the clarified supernatants were incubated for 6 h at 4° C with 20 μL of agarose beads conjugated to a polyclonal antibody against *c*-Myc. After four washes with 1× PBS (pH 7.4), the immunoprecipitates were resolved by 8% or 10% SDS-PAGE and immunoblotted with the anti-HA monoclonal antibody HA.11.

To immunoprecipitate endogenous MAVS, HEK293 cells stably expressing Myc-tagged CLPB were infected with or without SeV (4 HA units/mL) overnight at 37º C. The following day, the cells were washed once with 1× PBS (pH 7.4), lysed with lysis buffer containing 50 mM Tris-HCl (pH 7.4), 150 mM NaCl, 10% (w/v) glycerol, 1 mM EDTA, and 0.5% (w/v) digitonin, protease inhibitor cocktail, and the clarified supernatants were incubated with 2 mg of the anti-*c*-Myc monoclonal antibody 9E10 followed by incubation overnight at 4° C with 20 μL of protein A-Sepharose beads. The beads were washed four times with 1× PBS (pH 7.4), and the immunoprecipitates were resolved by 8% SDS-PAGE and immunoblotted with the anti-MAVS polyclonal antibody.

Cytochemical analysis of COX activity

COX staining was performed as previously described (Yoshizumi et al. 2017) with slight modifications.   In brief, cells plated on 18-mm coverslips were fixed with 2% paraformaldehyde in 1× PBS (pH 7.4) for 15 min and washed twice with 1× PBS (pH 7.4) for 5 min each.   To visualize COX activity, cells were stained with 100 mM phosphate buffer (pH 7.4) containing 0.6 mg/mL 3',3'-diaminobenzidine, 0.3 mg/mL cytochrome c, and 45 mg/mL sucrose for 2 h at 37° C.   Cells were then washed twice with 0.1 M Tris-HCl buffer (pH 8.0) for 5 min each and analyzed by microscopy.

Quantification and Statistical Analysis

Two-tailed Student's t tests were used for comparisons of two samples.   All statistical analyses were performed in GraphPad QuickCalcs (GraphPad Software).   Data are presented as mean ± standard error (SEM).   The statistical tests used and the number of biologic replicates is indicated in each figure legend.   Statistical significance was defined as a p value of less than 0.05.   No methods were used to determine whether the data met the assumptions of the statistical approach.

Data and Software Availability

Refined PHB2[188-265] crystal structure; Protein Data Bank (PDB ID: 6IQE)

BioID2 data [Control, PHB2(V1), PHB2(V3)]; Japan ProteOme STandard Repository/Database (jPOST) (JPST000527/PXD011939)

BioID2 data (PHB2[WT], PHB2[I225P], PHB2[KKK]); jPOST (JPST000529/PXD011946)

BioID2 data (MAVS, CLPB, PHB1); jPOST (JPST000618/PXD014218)

Cross-linking MS data; jPOST (JPST000528/PXD011941 and JPST000617/PXD014217)

Supplemental References

Adams, P.D., Afonine, P.V., Bunkóczi, G., Chen, V.B., Davis, I.W., Echols, N., Headd, J.J., Hung, L.W., Kapral, G.J., Grosse-Kunstleve, R.W., et al. (2010) PHENIX: a comprehensive Python-based system for macromolecular structure solution. Acta Cryst. D66, 213–221.

Edelhoch, H. (1967) Spectroscopic determination of tryptophan and tyrosine in proteins. Biochemistry 6, 1948-1954.

Emsley, P., Lohkamp, B., Scott, W.G., and Cowtan, K. (2010) Features and development of Coot. Acta Crystallogr. D Biol. Crystallogr. *66*, 486-501.

Gilquin, B., Taillebourg, E., Cherradi, N., Hubstenberger, A., Gay, O., Merle, N., Assard, N., Fauvarque, M.O., Tomohiro, S., Kuge, O., and Baudier, J. (2010) The AAA$^+$ ATPase ATAD3A controls mitochondrial dynamics at the interface of the inner and outer membranes. Mol. Cell. Biol. *30*, 1984-1996.

Janke, C., Magiera, M.M., Rathfelder, N., Taxis, C., Reber, S., Maekawa, H., Moreno-Borchart, A., Doenges, G., Schwob, E., Schiebel, E., et al. (2004) A versatile toolbox for PCR-based tagging of yeast genes: new fluorescent proteins, more markers and promoter substitution cassettes. Yeast *21*, 947-962.

Kabsch, W. (2010) XDS. Acta Crystallogr. D Biol. Crystallogr. *66*, 125-132.

Liu, F., Lössl, P., Scheltema, R., Viner, R., and Heck, A.J.R. (2017) Optimized fragmentation schemes and data analysis strategies for proteome-wide cross-link identification. Nat. Commun. *8*, 15473.

Lorenz, M.C., Muir, R.S., Lim, E., McElver, J., Weber, S.C., and Heitman, J. (1995) Gene disruption with PCR products in *Saccharomyces cerevisiae*. Gene *158*, 113-117.

Miyata, N., Goda, N., Matsuo, K., Hoketsu, T., and Kuge, O. (2017) Cooperative function of Fmp30, Mdm31, and Mdm32 in Ups1-independent cardiolipin accumulation in the yeast *Saccharomyces cerevisiae*. Sci. Rep. *7*, 16447.

Okuda, S., Watanabe, Y., Moriya, Y., Kawano, S., Yamamoto, T., Matsumoto, M., Takami, T., Kobayashi, D., Araki, N., Yoshizawa, A.C., et al. (2017) jPOSTrepo: an international standard data repository for proteomes. Nucleic Acids Res. *45*, D1107-D1111.

Tong, A.H., and Boone, C. (2006) Synthetic genetic array analysis in *Saccharomyces cerevisiae*. Methods Mol. Biol. *313*, 171-192.

Winn, M.D., Ballard, C.C., Cowtan, K.D., Dodson, E.J., Emsley, P., Evans, P.R., Keegan, R.M., Krissinel, E.B., Leslie, A.G., McCoy, A., et al. (2011) Overview of the CCP4 suite and current

developments. Acta Crystallogr. D Biol. Crystallogr. *67*, 235-242.

Yoshizumi, T., Ichinohe, T., Sasaki, O., Otera, H., Kawabata, S., Mihara, K., and Koshiba, T. (2014) Influenza A virus protein PB1-F2 translocates into mitochondria via Tom40 channels and impairs innate immunity. Nat. Commun. *5*, 4713.

Zhu, J., Vinothkumar, K.R., and Hirst, J. (2016) Structure of mammalian respiratory complex I. Nature *536*, 354-358.